Emergent Materials
https://doi.org/10.1007/s42247-021-00205-6

REVIEW

# Development of photovoltaic solar cells based on heterostructure of layered materials: challenges and opportunities

**Priyanka Das[1] · Sanjay K. Behura[2] · Stephen A. McGill[3] · Dharmaraj Raghavan[4] · Alamgir Karim[5] · Nihar R. Pradhan[1]**

Received: 19 January 2021 / Accepted: 8 March 2021


**Abstract**

Two-dimensional (2D) van derWaals layered materials created new avenue for the last decade in the field of optoelectronics for showing promising new and diverse applications. Strong light-matter interaction properties on these materials in single to few atomic layer form realized promising thinnest possible photovoltaic solar cells. Over the past few years, optoelectronics properties such as field-effect transistors, photodiodes, memory devices, optical switching, and excitonic physics of these materials have been intensively explored which indicates great potential for photovoltaic applications. Here, we reviewed the recent progress on photovoltaic solar cells of these 2D materials and their heterostructures with different device configurations. The p-n junction solar cells of vertical and lateral configuration devices are discussed in detail based on their stacking using mechanical transfer method or fabricated using CVD technique. The performance of each device configurations was also discussed based on their charge collection efficiency. In addition, we discussed the challenges and limitation of these photovoltaic solar cells and the possible routes to enhance the efficiency for future practical applications.

## 1 Introduction

The increasing demand of utilizing solar energy has attracted immense attention among all the renewable energy sources as the electrical energy necessary to meet the current requirement with growing population leads to the depletion of natural resources of fossil fuels which causes the detrimental effect on the global climate change [1]. Solar energy is already harnessed worldwide as different solar technologies including solar heating, solar thermal electricity generation, and solar photovoltaics [2]. Photovoltaics, which converts solar energy to electricity, is a practical and feasible solution to such challenges like energy crisis and environmental pollution [3]. Therefore, researchers have paid much attention to the photovoltaic (PV) technology to restore the remaining fossil fuels [4, 5]. The photovoltaic solar cells consist of hole rich materials (*p*-type) sandwiched with electron-rich material (*n*-type) to form most commonly used solar cell *p-n* junction. An intrinsic active layer (i) sandwiched between very thin *n*- and *p*- layers will form p-i-n junction solar cells. The doped layers define the built in potential and act as carrier collection layers. Sunlight converts into electricity through the generation of electron-hole pairs at the semiconducting p-n or p-i-n junctions in the solar cells. Meanwhile, PV technology based on thin film crystalline silicon (c-Si) photovoltaics which provides efficiency exceeding 20% has been recognized due to its commercial mass production to meet the industrial demand and to produce electronics module [6–8]. However, a new generation of electronic devices for flexible and wearable electronics is required which can combat the conventional rigid Si- semiconductor technology as the high cost of crystalline silicon and the manufacturing process sometime limits its practical use [9–11]. Additionally to meet the low cost and simple fabrication methods, photovoltaic cells based on inorganic-organic charge transport materials, e.g, $TiO_2$ [12, 13],

✉ Nihar R. Pradhan
nihar.r.pradhan@jsums.edu

1 Department of Chemistry, Physics and Atmospheric Sciences, Jackson State University, 1400 John R. Lynch Street, Jackson, MS, USA

2 Department of Chemistry and Physics, University of Arkansas, Pine Bluff, AR, USA

3 National High Magnetic Field Laboratory, Tallahassee, FL 32310, USA

4 Department of Chemistry, Howard University, Washington DC, USA

5 Department of Chemical & Biomolecular Engineering, University of Houston, Houston, TX, USA

Published online: 11 May 2021

copper indium gallium selenide (CIGS) [14], perovskite [15], gallium arsenide (GaAs) [16] including dye-sensitised solar cells (DSSCs) [17], quantum dot (QD)-sensitized solar cell [18], and organic photovoltaics (OPVs) [19], [20, 21] are reported by several research groups as an alternative to silicon solar cells. The efficiency is still lower for DSSCs, OPVs, whereas the lab scale efficiency is reported quite higher for perovskite solar cells (~ 20% - 25%) [22]. However, the lower stability of the DSSCs and perovskite material in the environment restricts its wide practical application in PV technology [23, 24]. To make solar energy to electricity conversion practically and economically viable, the development of low-cost semiconducting material is important. The discovery of monolayer graphene in 2004 has led to the invention of a large number of other 2D materials. Graphene is a material with exceptionally high electrical conductivity, carrier mobility and optical transparency which has been used extensively in photovoltaics, flexible electronics etc. [25, 26]. Graphene (due to its zero bandgap) has successfully implemented in the several metal/semiconductor interface for photovoltaic device application [27, 28]. Due to high electrical conductivity, flexibility and transparency graphene has been used widely as organic photovoltaics (OPVs) for indoor application. These OPVs including graphene, their polymers exhibits incredibly good stability in indoor air condition and has exceeded a power conversion efficiency ~ 26% under indoor condition. The OPV modules including graphene and 2D materials with various advantage made those promising for practical applications [29, 30]. Along with graphene (zero bandgap), an enormous number of 2D layered materials have been emerged and recently attracted extensive attention in new generation electronic devices due to its tunable bandgap from indirect to direct bandgap with decreasing layer thickness [31], [32]. 2D semiconductors are used as interface materials in perovskite photovoltaic solar cell to reduce the carrier trap density [33, 34]. Those 2D materials crystals can be synthesized through a simple, cost-effective technique such as chemical vapor transport (CVT) or chemical vapor deposition (CVD) [35, 36]. However, there is a large emphasis to develop alternative growth technique of 2D materials which will be promising for large area device application. Therefore, the synthesis of 2d material thin films using the techniques like Pulsed Laser Deposition (PLD), Molecular Beam Epitaxy (MBE), sputtering method etc. are reported elsewhere [37–40]. The deposition of monolayer to few layered $MoS_2$ thin film on sapphire (0001) substrate through PLD technique is reported by Siegel et al. where they discussed that the number of layers can be controlled by controlling the number of pulses in a PLD process [41]. The synthesis of few layered $MoS_2$ film on amorphous boron nitride buffered silicon substrates through magnetron sputtering is reported by Samassekou et al. [42]. They investigated the structural, optical and transport properties of the synthesized $MoS_2$ films which represented a good conductivity and photoresponse behavior. The successful growth of *h*-bN on graphene on Ni (111) substrate to make *h*-bN / graphene heterostructure through MBE technique is reported by Wofford et al. [43]. Therefore, the synthesis of large area 2D materials film through these deposition techniques opens a new path for the application in electronics and device application which sometimes necessary compared to irregular shaped 2D material flakes which are not scalable for large area device application. One can extract these layered 2D materials from their bulk crystal through mechanical or chemical exfoliation as the atoms are bonded together with strong in-plane covalent bond and weak van der Waals bond in between the layers [44, 45]. The structure-property relation, electronic properties of the 2D materials were revealed by many researchers [46, 47].

Among semiconducting 2D layered materials, transition metal dichalcogenides (TMDCs) including $MoS_2$, $WS_2$, $MoSe_2$, $WSe_2$ etc. and black phosphorus (bP) are studied a lot as those materials exhibit unique optical, electrical, chemical, thermal, mechanical properties at its atomic scale thickness compared to its bulk counterpart [48–52]. These TMDCs exhibit strong light-matter interaction at their atomic level which gives a excellent platform to study the optoelectronic properties under solar spectrum [53, 54]. Having this extraordinary optical, electronic properties with decreasing layer thickness, TMDC family has been considered as an important material for optoelectronic applications [55]. Importantly, the strong light-matter interaction property, layer-dependent tunable bandgaps at few to single layer thickness of these semiconducting 2D materials enable them as a potential candidate for photovoltaic applications. The surface of layered 2D materials does not have any dangling bond which unfolds an innumerable prospect to fabricate diverse *p-n* junction heterostructures composed of different layers of 2D materials despite their lattice mismatch for different materials [56]. Those heterostructures are studied by many researchers to understand their optoelectronic behavior and the applications in photovoltaics [57]. Here, we review the different types of *p-n* junction heterostructures based on their device geometry and specifically their corresponding application in photovoltaic solar cells. In Section 3, the parameters that are highly important to describe the photovoltaic performance are discussed briefly. Section 4 describes the type of different *p-n* heterostructures based on the device configuration. In Sections 5, 6, and 7, the efforts made by many researchers to prepare different heterojunction devices to understand photovoltaic performances in individual device geometry are described.

In Section 8, we discuss the challenges and opportunities of those *p-n* junction heterostructure devices towards the practical application in photovoltaic technology.

## 2 Photovoltaic metrices

The set of parameters to evaluate the photovoltaic performances are determined from the *I-V* characteristics of the device under light illumination condition. For a reliable measurement of *I-V* characteristics, the measurements are performed under a standard test condition (STC), where the total solar irradiance is equal to 1000 W/m$^2$ and the incident light is standardized under AM 1.5 solar solar spectrum. Here in this section, we will introduce the photovoltaic parameters briefly.

The *short-circuit current* ($I_{sc}$) is the current that flows through the external circuit of a device when there is no applied voltage between the two terminals, i.e., two terminals are short circuited. The short-circuit current of a photovoltaic device depends on the photon energy of the incident light spectrum. The standard spectrum of AM 1.5 solar spectrum is generally used to evaluate the photovoltaic parameters. The term *short-circuit current density* ($J_{sc}$) is used very often to remove the solar cell area dependency on $I_{sc}$, which actually determined the maximum output current from a solar cell. The general unit of $J_{sc}$ is A/cm$^2$.

The *open-circuit voltage* ($V_{oc}$) is another important parameter which defines as an electrical potential difference across a solar cell when no current is flowing through the circuit ($I = 0$). $V_{oc}$ represents the maximum output voltage form a solar cell. It corresponds to the forward bias voltage of the solar cell at which photogenerated current is compensated by dark current.

Another important parameter *fill-factor* ($FF$) is the ratio of maximum electrical output power ($P_{el}^{max}$) generated from solar cell to the product of $J_{sc}$ and $V_{oc}$. However, one can get the electrical output power ($P_{el}$) by multiplying current and voltage. The output power ($P_{el}$) is zero at any of the condition of short-circuit current ($V = 0$) or open-circuit voltage ($I = 0$). The maximum output power ($P_{el}^{max}$) is the product of $I_{MP}$ and $V_{MP}$, where $I_{MP}$ is the current at maximum power point and $V_{MP}$ is the voltage at maximum power point. The unit of power is expressed in watt (W). Fill factor (FF) can be represented by Eq. 1.

$$FF = \frac{P_{el}^{max}}{J_{sc}V_{oc}} = \frac{I_{MP}V_{MP}}{J_{sc}V_{oc}} \tag{1}$$

Fill factor determines the maximum power of a solar cell and it is dimensionless quantity.

Power conversion efficiency ($PCE$) is defined as the ration between maximum generated power to the incident optical power ($P_{in}$) which can be represented by Eq. 2.

$$PCE = \frac{P_{el}^{max}}{P_{in}} = \frac{J_{sc}V_{oc}FF}{P_{in}} \tag{2}$$

It is also a dimensionless quantity (expressed as %) and it resembles to the percentage of light energy converts to its electrical energy by a photovoltaic device.

## 3 Device geometry of heterostructure-based *p-n* junction photovoltaic solar cells

Photovoltaic effect depends on the *p-n* junction or Schottky barrier junction which produces built-in electric potential to separate photogenerated electron-hole carriers. Depending on the device geometry, the 2D heterostructure photovoltaic devices can be classified into two categories: (1) lateral configuration where the built-in electric field is in the in-plane direction of 2D material, another is (2) vertical configuration where the electric field is in the perpendicular direction of the plane of 2D materials.

Depending upon the charge carrier collection from the *p-n* junction region and the way *p-n* junction was formed, we sketched 4-different geometry of 2D material–based heterostructure photovoltaic *p-n* junction solar cells. Figure 1 shows the 4-configuration of 2D heterostructure *p-n* junction solar cells. Figure 1a shows the vertical *p-n* junction solar cell where two different layered materials with opposite polarity placed on the top of each other overlapping partially to form the vertical heterostructure. The active *p-n* junction area is the overlapping area of both the materials. In this vertical *p-n* heterostructure geometry, electron-hole pairs are generated vertically in the two different 2D materials by illuminating the channel with light source, but they travel laterally to the contacts away from the junction for collecting the photovoltaic current. Figure 1b shows a second vertical *p-n* junction heterostructure device, where two graphene metal contacts (top metal contacts should be transparent for illuminating the junction) are placed both side (bottom and top) of the heterojunction area of *n*- and *p*-type materials. Thus, the carriers that generate from this type of heterojunction will directly move to the contacts placed on the top of the each flake without moving laterally. Thus, the charge carrier injection/collection efficiency in this device geometry expected to be better than the device geometry in Fig. 1a which eliminates the effect of lateral resistance of the channel on the mobility of the charge carriers.

Due to the planner and thin geometry of the 2D materials, it is easier to modulate the charge carrier density in the channel. Using a dual gate geometry, one can control/accumulate the charge locally in the channel to built *n*-type or *p*-type region in the same materials as shown in

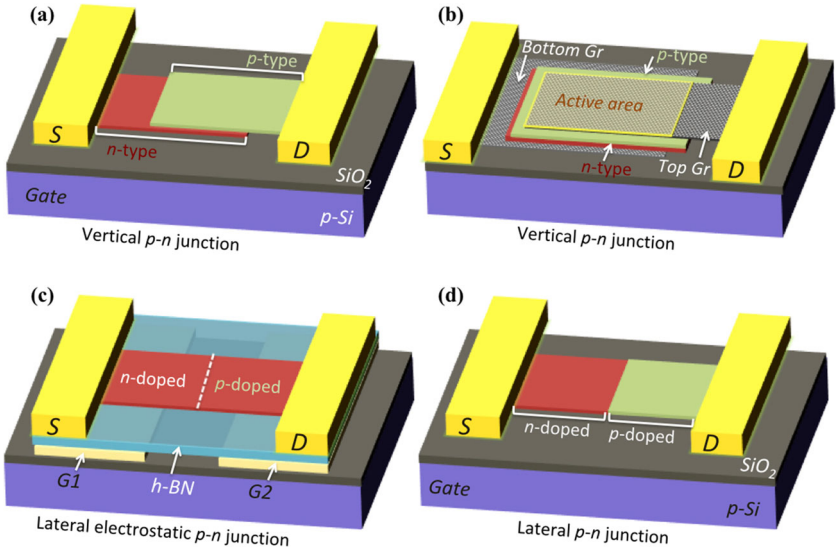


**Fig. 1** Schematic of different types of *p-n* junction based on 2D materials. **a** Vertical *p-n* junction formed by *n*- and *p*-type materials, where carriers are measured laterally away from the junction area. **b** Vertical *p-n* junction with *p*- and *n*-type materials sandwiched on the top of each other where carriers are measured across the junction. **c** Electrostatic lateral *p-n* junction formed by dual gating geometry where half of the channel can be doped with holes and other half with electron. **d** Lateral *p-n* junction can be formed using CVD grown method where *p* or *n*-type materials can be grown laterally to form *p-n* junction devices

the schematic of Fig. 1(c). The opposite polarity of gate voltages will be applied by the gates G1 and G2 to induce a sharp electron and hole doping junction to the channel to form the *n*- and *p*-type region and separated by a small gap to form a perfect *n-p* junction. The gates are separated from the channel with high-$\kappa$ *h*-BN dielectric layers. The separation gap of two gates defines the junction area. The formation of lateral *p-n* junction is due to the applied electric field by the gate voltages and it is called as electric field–induced *p-n* junction device. The last geometry we will discuss in this review chapter is the lateral *p-n* junction photovoltaic solar cell grown via CVD method. With certain growth condition, one can grow the *n*- and *p*-type materials one after another on a plane in a sequential pattern, stitching together on a substrate to form *p-n* junction. In this method, two different polarity of the materials grown one after another along a plane where second materials will stitch from the terminated position of first materials to form sharp lateral *p-n* junction heterostructure. In the following sections, we will discuss the recent development on photovoltaic effect based on different heterostructure geometries of 2D materials.

## 4 Vertical *p-n* junction heterostructure solar cells

Among the several group of 2D semiconducting layered materials, a group of materials such as $MoS_2$, $MoSe_2$, and $WS_2$ shows *n*-type conduction whereas several other materials such as $MoTe_2$, $WSe_2$, and BP show intrinsic *p*-type behavior. A vertical *p-n* junction can be made by simply stacking two flakes together of opposite polarity. Furchi et al. [58] reported a type II vdW heterosturcture composed of $MoS_2$ and $WSe_2$ monolayers which were mechanically exfoliated on 285 nm $Si/SiO_2$ substrate individually and then one of them lifted up and transferred onto the other to make a vertically stacked heterostructure. In their device geometry, the contacts are on both sides of the junction far from the active area of the *p-n* junction heterostructure, where charge carriers and electron/holes will generate in the active area in vertically stacked overlapping region and then travel to the metal contacts laterally. This device structure is similar to the one discussed in Fig. 1a. The reported photovoltaic efficiency from this monolayer $MoS_2/WSe_2$ device is $\sim$ 0.2%. This low efficiency was due to the low absorption of monolayer samples and the method used for extraction of charge carriers from the photovoltaic junction, where the carriers can travel laterally from the junction and suffer with scattering mechanism and interlayer recombination process. On the other hand, author estimated that if the extraction of the charge carriers were done by vertically stacked electrode on both sides of the stacking layers of $MoS_2/WSe_2$, they could achieve $\sim$1% efficiency, which is 5 times higher than the measured values.

Similarly, Cheng et al. [59] demonstrated excellent current rectification behavior of few layer $MoS_2/WSe_2$ heterojunction at zero gate voltage with an ideality factor of n = 1.2. Figure 2c displays the measured $I_{ds}$ as a function of $V_{ds}$ of the heterojucntion at several applied back gate voltages shows rectification of current/diode like characteristic. Figure 2d shows the logarithmic plot of drain-source current at $V_g$ = 0 V and −20 V. The dotted lines are fitting to the diode equation. The extracted ideality factor is $n$ = 1.2 which shows perfect diode-like behavior. Figure 2e exhibits the output characteristics of the heterojunction in both dark and laser illumination power of 5 $\mu$W of

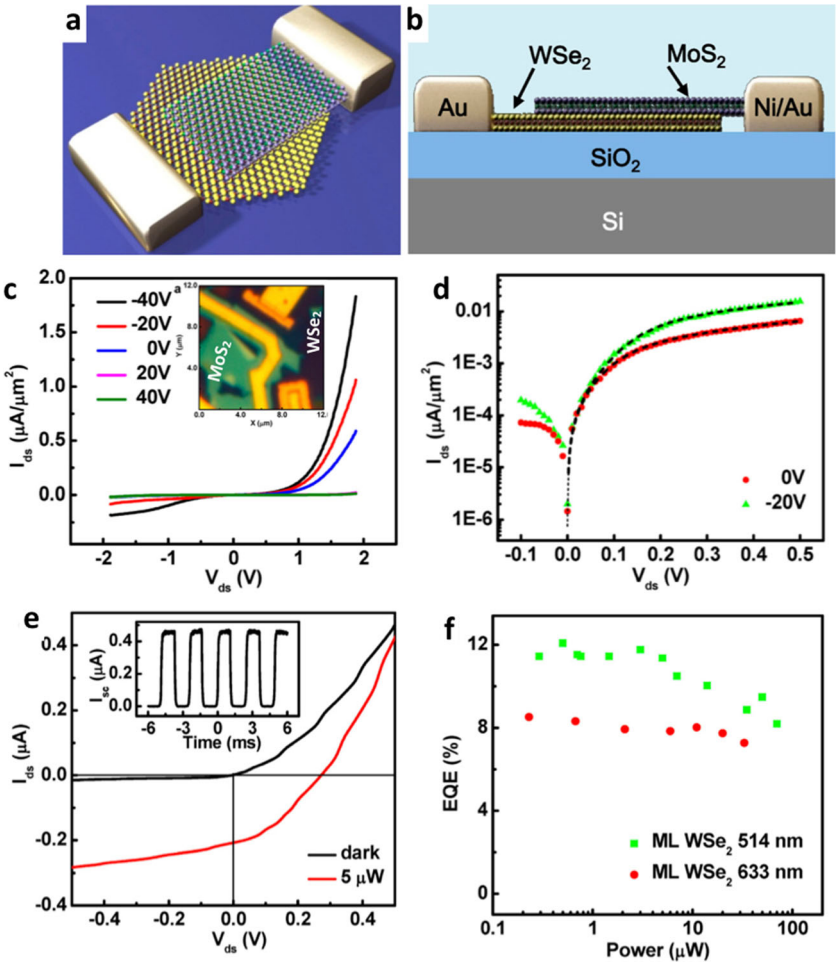


**Fig. 2** $MoS_2/WSe_2$ vertical heterostructure. **a** and **b** are top view and side view of the schematic of the heterostructure. **c** shows the $I_{ds}$ vs $V_{ds}$ of the heterostructure device of the optical image shown in the inset. **d** Logarithmic plot of $I_{ds}$ vs $V_{ds}$ shows rectification of the current and dotted lines are the fitting to the diode equation. **e** $I_{ds}$ vs $V_{ds}$ with (red) and without (black) light illumination with 5 $\mu$W laser power of $\lambda = 514$ nm. **f** Power-dependent EQE of the heterojunction at $V_{ds} = 0$ V and $V_g = 0$ V. Reproduced with the permission from reference [59]

514-nm wavelength, which shows a photovoltaic effect with an open-circuit voltage ($V_{oc}$) of 0.27 V and short-circuit current ($I_{sc}$) of 0.22 $\mu$A. Inset of Fig. 2e shows the photocurrent response of the *p-n* junction at excitation power of 10 $\mu$W. The maximum EQE value was found to be of 12% obtained at excitation power of 0.5 $\mu$W. The higher the EQE value, the better the photovoltaic response as it defines the number of electron-hole pair generation by number of incident photons. A high photovoltaic quantum efficiency of $> 50\%$ based on ultrathin *p-n* heterojunction of $WSe_2/MoS_2$ was achieved by Wong et al. [60]. The authors demonstrated that by systematically engineering the bandgap of the active layer and the metal contacts, an experimental absorbance exceeding 90% was achieved which was in good agreement with their electromagnetic simulation results.

The above discussion, based on the atomic layer vertical *p-n* junction devices, displays photovoltaic responses where the collection of charge carriers or metal contacts is far from the junction area. Even though the efficiency of the atomic layer–stacked *p-n* junction devices are poor, they are potential candidates for electroluminescence due to the nature of direct bandgap. Lee and coworkers reported two types of atomically thin *p-n* junctions by stacking a single to few layers of $MoS_2$ on the top of thin layer of $WSe_2$ through dry mechanical transfer technique [61]. In one case, the charge collection was done laterally far away from the junction as discussed above and in the second device, the photogenerated carriers were collected from the top of the device by putting the 2D metallic contacts. Figure 3a shows the schematic representation of the device geometry where bottom right panel shows the optical image of the fabricated device. The device is composed of vertically stacked monolayers of $WSe_2$ and $MoS_2$. The metal contacts are connected laterally as discussed before. Figure 3b displays the drain-to-source current ($I_{ds}$) as a function of applied drain-to-source voltage, $V_{ds}$, at various applied gate voltages between the metal contacts on the $WSe_2$ (D1) and $MoS_2$ (S1). The *p-n* diode exhibits promising gate-tunable current rectification as electrostatic doping modulates the carrier density. The inset in Fig. 3b shows the individual FET behavior of $MoS_2$ and $WSe_2$ indicates *n*-type and *p*-type conduction. The photoresponse behavior of the device under white light illumination is shown in

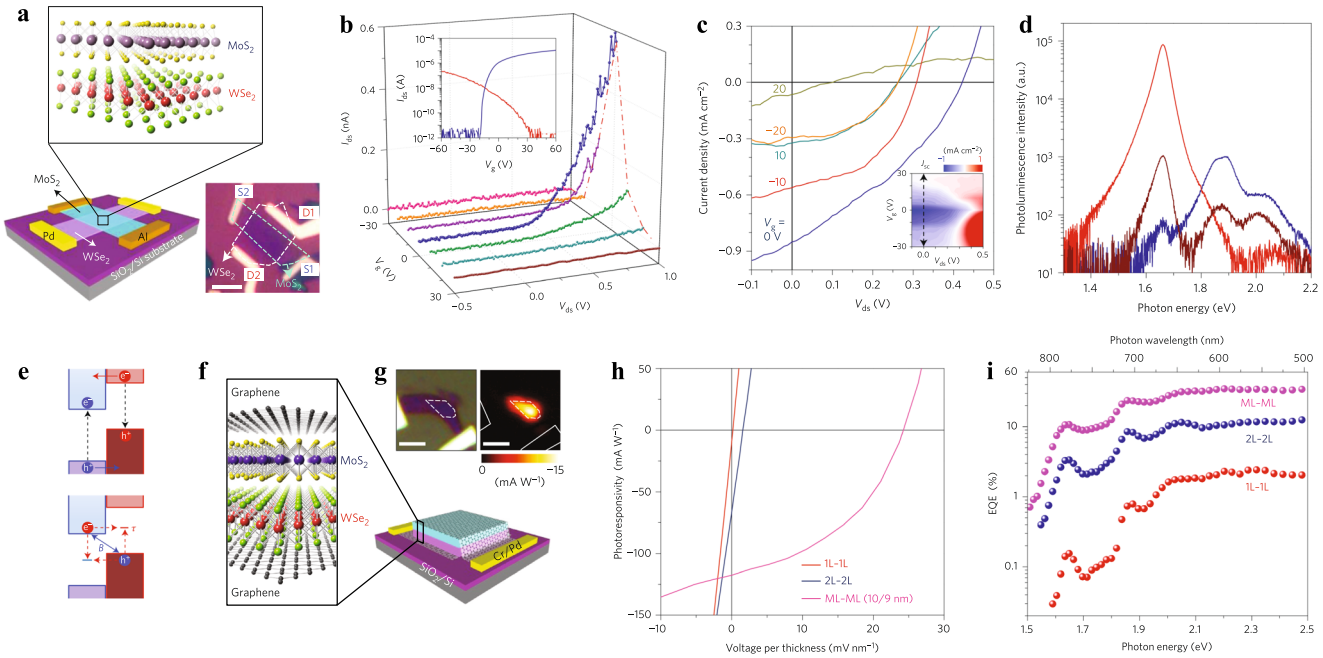


**Fig. 3** **a** Schematic diagram of $MoS_2/WSe_2$ van der Waals heterostructures device with lateral metal contacts. Optical image of the fabricated device is shown in bottom right. **b** $I_{ds}$–$V_{ds}$ curves of the device at different gate voltages across the junction. **c** Photoresponse behavior with varying gate voltages under white light illumination. **d** Photoluminescence spectra of the isolated monolayers (blue curve for $MoS_2$; red curve for $WSe_2$) and the overlapped *p-n* junction region (brown curve). **e** Schematic description of exciton dissociation. **f–g** Schematic diagram of top and bottom graphene sandwiched $MoS_2/WSe_2$ device and the photocurrent map, respectively. **h–i** Photoresponse characteristics of the graphene sandwiched device and EQE plots as a function of excitation energy with varying thickness, respectively. Reproduced with the permission from reference [61]

Fig. 3c in the gate range of of −30 to 30 V. The measured current density as a function of applied drain-source voltage at fixed $V_g = -20$ V to 20 V shows photovoltaic response. To understand the nature of this heterostructure, PL was measured and compared with the PL of individual flakes. Figure 3d shows the photoluminescence spectra of the individual monolayer and the corresponding *p-n* junction. The photoluminescence intensity decreases strongly in the $MoS_2/WSe_2$ junction region compared to its individual monolayer which proved the efficient charge transfer process between $MoS_2$ and $WSe_2$ layers at the junction. The tunable optoelctronic property is obtained due to the tunneling-assisted interlayer recombination of majority charge carriers. To increase the carrier mobility and also before they can be collected to reduce interlayer recombination losses, the author sandwiched the device in between the graphene layers to collect the carriers directly from the junction through vertical charge transfer, which enhanced the charge carrier collection. The schematic design of the graphene-sandwiched device and the corresponding optical image, photocurrent map is shown in Fig. 3g. The photovoltaic response of the sandwiched *p-n* junction with varying thickness is presented in Fig. 3h. Figure 3i displays the measured external quantum efficiency (EQE) as a function of excitation energy. The diode resulted highest EQE of 34% for multilayer *p-n* junction at 532 nm.

The low mobility in the lateral collection of charge carrier devices is due to the diffusion of majority charge carriers between the junction when they leave and the collection point (metal contact point). The diffusion life time in this lateral collection method is so small, $\sim 1\ \mu$s, because it always competes with the interlayer recombination process and that limits the efficiency of the photovoltaic solar cell in this device. Thus, to increase the rate of charge collection, the author demonstrated using graphene as a contact on both sides of the junction (Fig. 3f). This allows increase of carrier collection by direct vertical charge transfer rather than through lateral diffusion. This geometry would be ideal *p-n* junction solar cell based on 2D semiconductors.

One of the major requirements to achieve enhanced photovoltaic effect (or efficiency) is the balance of charge carrier mobility of both *n*- and *p*-type materials used for *p-n* junction device. Kwak et al. investigated *p-n* junction photovoltaic devices based on heterostructure of $bP/WS_2$, where $WS_2$ have *n*-type and bP shows *p*-type conduction [62]. Figure 4a shows the optical image of the $bP/WS_2$ heterojunction device. The exfoliated $WS_2$ and bP multilayers are used in this heterojunction device to enhance the light-absorption properties because the thick 2D materials can generate more electron–hole pairs than those of ultrathin layers. The thickness of $WS_2$ and bP used in this device is 12 nm and 10 nm respectively.

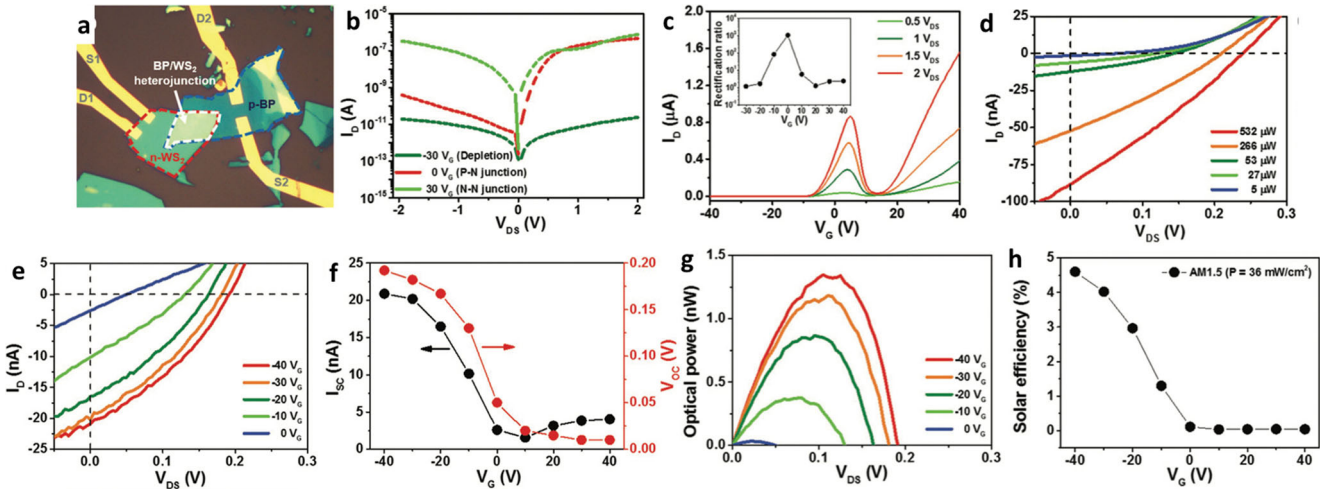


**Fig. 4** Photovoltaic effect of bP/$WS_2$ heterpstructure p-n junction. **a** Optical image of the bP/$WS_2$ *p–n* heterojunction device. **b** drain-source current as a function of drain-source voltage of the junction at gate voltage $V_G = -30$ V, 0V and 30 V, respectively. **c** Transfer curve of the bP/$WS_2$ *p–n* heterojunction device with applied different gate voltages. Inset shows the rectificaion behavior as a function of gate voltage. **d** *I-V* curve of the junction using laser light illumination from λ = 405 nm at several applied optical power shows photovoltaic response. **e** *I-V* curve of the bP/$WS_2$ *p–n* heterojunction device with applied different gate voltages under AM 1.5 light illumination. **f** Extracted short-circuit current and open-circuit voltage of the heterojunction as a function of gate voltage, obtained from (e). **g** Output optical power vs drain-source voltage at different gate voltages. **i** Efficiency of the *p-n* junction solar cell as a function of applied gate voltage obtained from AM 1.5 light illumination. Reproduced with the permission from reference [62]

The electrical FET characterization of bP shows ambipolar with high *p*-doped characteristic and $WS_2$ shows *n*-type behavior. The drain-source current ($I_D$) as a function of drain-source voltage ($V_{DS}$) presented in Fig. 4b indicates the output characteristic of *p-n* junction device at depletion ($<-10$ V) and *p-n* ($-5$ V to 10 V) and *n-n* junction ($>$ 20 V). These three regions are indicated from the FET charcateristic of bp/$WS_2$ heterojunction shown in the Fig. 4c. In the *p-n* junction region (red line in Fig. 4b), a strong diode-like rectification of current in the order of $10^3$ is observed at $V_G$ = 0 V. Figure 4d presents the *I–V* curves of the bP/$WS_2$ heterojunction device measured at several fixed illuminated optical powers from 5 to 532 $\mu$W. Short-circuit current ($I_{sc}$) and open-circuit voltage ($V_{oc}$) increase as a function of increasing optical power. Authors calculated the charge carrier density for both electron and holes in this bP/$WS_2$ heterostructure as a function of gate voltage to understand the balance of the charge carrier with and without optical power illumination. The balance point (crossing point) of charge carriers, where both the density of electrons and holes matches, can shift with the applied optical power due to the doping effect. The photovoltaic effect also observed to be maximum at the applied gate voltage where the charge carriers are balanced [62]. Figure 4e–h present the photovoltaic effect of bP/$WS_2$ heterojunction under an AM 1.5 solar spectrum. Figure 4e displays the *I-V* curve of the heterojunction at 36 mW/$cm^2$ optical power illumination. The bP/$WS_2$ junction exhibits a strong photovoltaic response as a function of gate voltage with maximum value that appears at $V_G$ = -40 V. Figure 4f shows the $I_{sc}$ and $V_{oc}$ as a function of gate voltage. The extracted photovoltaic electrical power was calculated and presented as a function of drain-source voltage at several fixed gate voltages. The maximum electrical power obtained from this bP/$WS_2$ heterojunction device is 1.3 nW. Thus, the balance point of the charge carrier is confirmed at $V_G$ = -40 V, which shifted more in AM 1.5 white light illumination compared to the laser light of λ = 405 nm. Figure 4h presents the solar cell efficiency of bP/$WS_2$ heterojunction calculated from the relation $\eta = P_{max}/P_{in}$ plotted as a function of applied gate voltage. The maximum efficiency was obtained as 4.6% at $V_G$ = -40 V, under AM 1.5 solar spectrum of 36 mW/$cm^2$. The higher efficiency obtained in this device is due to the broadband light absorption of the heterojunction using low bandgap materials bP. Few layer bP can absorb the light at the infrared region where $WS_2$ can absorb at whole visible region of the solar spectrum. The efficiency on this BP/$WS_2$ heterosjunction could be enhanced further by stacking a metal electrode such as transparent electrode like graphene to collect the charge carriers directly from the junction as shown in the schematic of Fig. 1b instead of collecting them laterally, away from the junction as shown in the Fig. 4a.

The vertical heterostructure can be designed using doping technique on a multilayer crystals. If the *n-* or *p*-type semiconductor channel consists of several atomic layers, few layers on the top can be chemically doped with opposite polarity in a controlled fashion compared to the bottom layers

to achieve a vertically *p-n* junction device on the same material. Here, we are presenting a similar work by Li et al. [63] described a chemically doped vertical $MoS_2$ *p-n* junction where they used $AuCl_3$ and benzyl viologen as dopants to dope top-few layers of $MoS_2$ to *p*-type. $AuCl_3$ was used as a *p*-type dopant whereas benzyl viologen was used to enhance the *n*-type carriers in $MoS_2$. Figure 5a shows the graphical design of the $MoS_2$ device after doping with $AuCl_3$ and followed by annealing. The actual thickness of the $MoS_2$ *p-n* homojunction was experimentally found as 3 nm where the chemical doping depth found as 1.5 nm. The current-voltage characteristics of the homojunction were measured at $V_G = -60$ V to 60 V which is shown in Fig. 5b. All the curve shows rectification phenomena at positive bias voltage without any increase of current at negative bias which confirms the formation of *p-n* junction. The inset of Fig. 5b shows the logarithmic plot at $V_G$ = 60 V and red dotted line shows the diode fit, which yields ideality factor, $n = 1.6$. Figure 5c displays the *I-V* characteristic at $V_G = 0$ V without illumination of light showing diode-like rectification at positive bias. Inset shows the logarithmic plot of *I-V* data with and without illumination of light, which shows change in diode rectification as well as photovoltaic effect. Figure 5d shows the zoomed-in graph of current density as a function of drain-source voltage in linear scale to elucidate the photovoltaic effect clearly. At input optical power of $P_{in} = 100$ mW/cm$^2$, the device shows short-circuit current density $J_{SC} = 3.0$ mA/cm$^2$ and open-circuit voltage $V_{OC} = 0.6$ V. The device exhibited photovoltaic efficiency of $\eta = 0.4\%$ and fill factor (FF) value of 0.22 (Fig. 5d).

**Vertical vs lateral transport in *p-n* junction** As we discussed above that the efficiency of the device depends upon the charge collection mechanism from the *p-n* junction heterostructure, here, we discussed the results of lateral and vertical charge collection from a vertical *p-n* junction heterostructure. The *p-n* heterojunction based on bP/$MoS_2$ is reported by Miao et al. [64] where the authors compared the photovoltaic performance of the vertical *p-n* heterojunction with its partially overlapped bP and $MoS_2$ where charge carriers are collected laterally away from the junction area as discussed in Fig. 1a. Figure 6a displays the schematic of the vertical *p-n* diode where top and bottom electrodes are connected directly to the bP and $MoS_2$ layers. Figure 6b and c are the optical images of the fabricated vertical and lateral bP/$MoS_2$ *p-n* junction devices. Figure 6d and e are the corresponding AFM images indicated the $MoS_2$ and bP layers. The vertical heterojunction was found to be more stable in air compared to its lateral one as in vertical stack the ambient degradation of bP layer was retarded by $MoS_2$ layer. Both the device configuration showed excellent current rectifying behavior at zero gate bias as shown in the Fig. 6f. However, the vertical heterojunction resulted the current density much higher (~ 29.4 A/cm$^2$) compared to its lateral structure (~ 0.43 A/cm$^2$). The difference of current transport mechanism

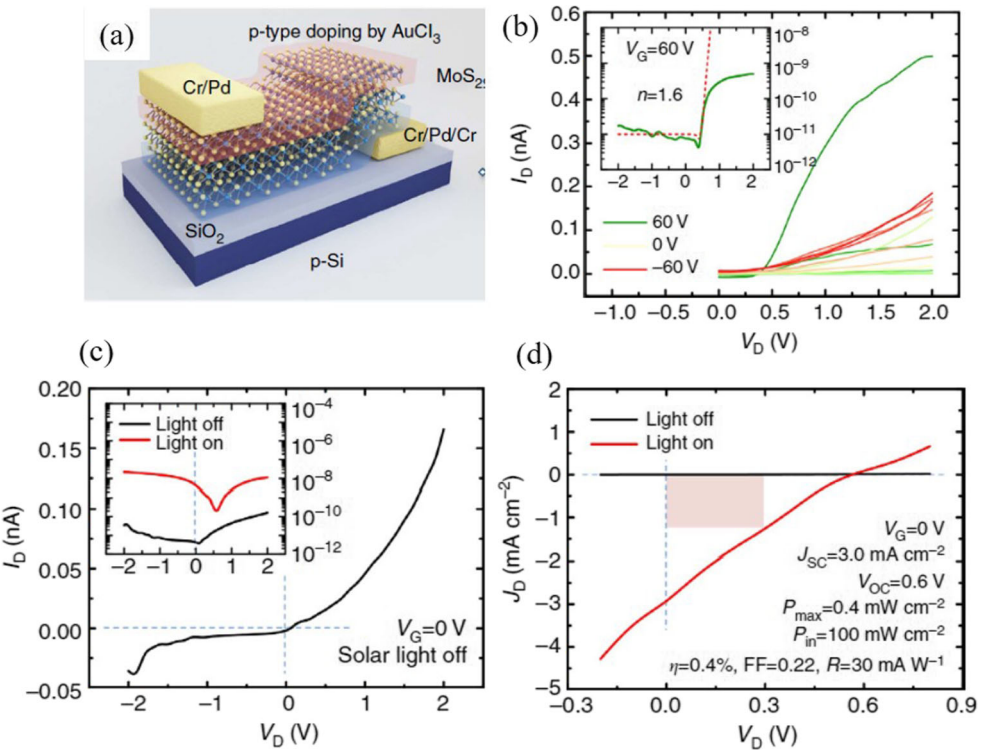


**Fig. 5** **a** Graphical design of the $MoS_2$ device chemically doped by $AuCl_3$. **b** Output characteristics of the device between $V_G$ range of −60 V to 60 V. Inset displays the output characteristics (logarithmic scale) of the device in its current-on state. **c** Photovoltaic performance of the device at $V_G = 0$ under standard solar light illumination. **d** Current density ($J_D$) plot as a function of drain source voltage ($V_D$) represents the energy conversion properties. Reproduced with the permission from reference [63]

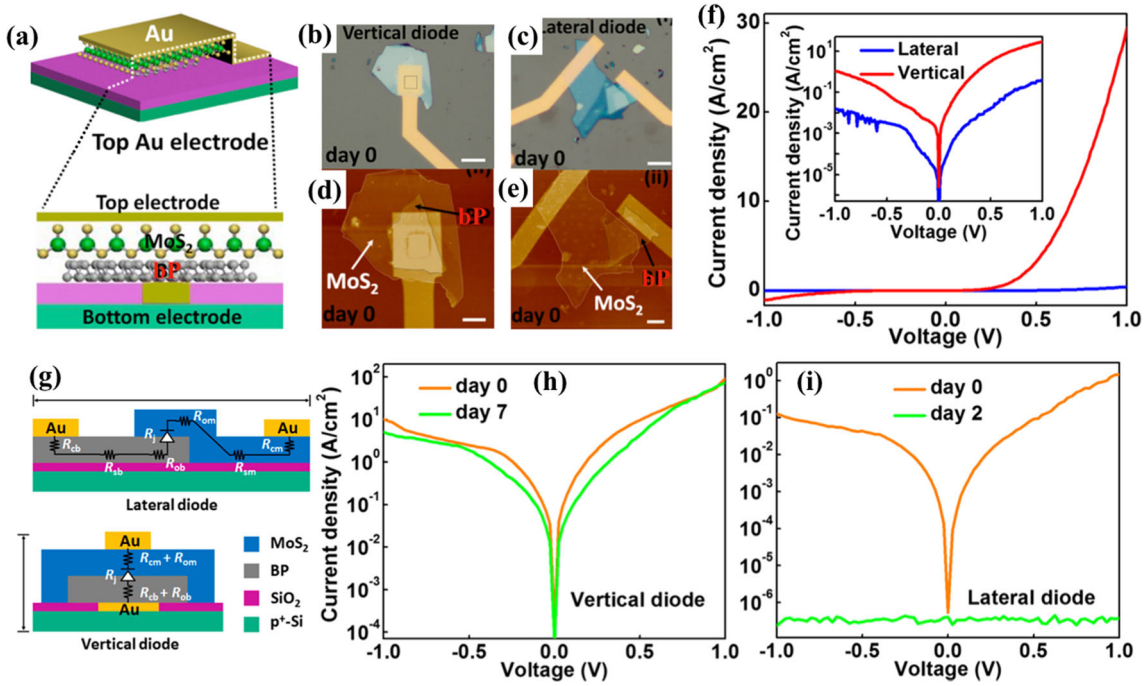


**Fig. 6** **a** Schematic view of the vertical bP/$MoS_2$ heterostructure device with cross sectional view at the bottom. **b** and **c** Optical images of vertical bP/$MoS_2$ heterojunctions diode in vertical and lateral configurations, respectively. d–**e** Corresponding AFM images of the vertical and lateral devices. **f** *p-n* junction diode characteristic shows current density as a function of applied voltage in lateral and vertical configurations. Inset shows the semilogarithmic scale plot of the same *I-V* curves. **g** Schematic diagram of the device model with all the circuit resistances of the lateral and vertical geometry of *p-n* junctions. $R_j$ represents the junction resistance of the bP/$MoS_2$ *p-n* junction, $R_{om}$ and $R_{ob}$ correspond to the $MoS_2$ and bP resistance in the overlap region, $R_{sm}$ and $R_{sb}$ represent the $MoS_2$ and bP series resistance outside the overlap region, and $R_{cm}$ and $R_{cb}$ are the contact resistance between $MoS_2$ or bP and the gold electrode. Ambient stability study of **h** vertical and **i** lateral bP/$MoS_2$ heterojunction *p-n* diodes. Reproduced with the permission from reference [64]

between these two geometry of devices is discussed below with the help of schematic diagram of different resistance associated with the devices. As illustrated in Fig. 6g, the total resistance in lateral configuration is divided into four parts: (1) resistance between bP/$MoS_2$ *p–n* junction at the interface ($R_j$), (2) the sheet resistances of bP ($R_{ob}$) and $MoS_2$ ($R_{om}$) in the overlapped region, (3) the series resistance of bP ($R_{sb}$) and $MoS_2$ ($R_{sm}$) outside the overlapped region, and (4) the contact resistances of metal with bP ($R_{cb}$) and metal/$MoS_2$ ($R_{cm}$). The resistance $R_j$ mainly contributes the rectification phenomena of the diode associated in both the configurations of the device geometry. In addition to this, sheet resistance and contact resistance associated with both geometry are similar since same metal contacts and similar thickness of the 2D flakes are used to fabricate the devices. The only difference that comes from these two device geometry is the series resistance ($R_{sb}$ and $R_{sm}$) in the lateral heterostructure geometry which is drastically different and additional compared to the vertical heterostructure geometry. For vertical heterostructure, charge carriers will travel across a very thin distance of the materials, which is the thickness of bP or $MoS_2$ without any series resistance. In contrast for a lateral heterostructure, charge carriers will go through laterally from the junction area (few micron) to reach the contacts under the influence of huge series resistance without any gate bias. This limits the output current in the lateral heterostructure geometry compared to the vertical *p-n* junction. Figure 6h and i display the ambient stability of the vertical and lateral heterojunction, respectively. Vertical heterojunction shows great stability due to the bP layer (which is vulnerable to the oxygen atmosphere) covered with the $MoS_2$ layer and protect from the degradation of the ambient atmosphere. In case of lateral *p-n* junction device, bP can degrade quickly due to the exposure to the oxygen atmosphere which destroys the device completely within few hours [65]. Thus, this work demonstrated the potential application of vertical *p-n* junction heterostructure for photovoltaic solar cell applications.

Additionally, vertical heterojunctions made of other 2D crystals, e.g, $\alpha$-$MoTe_2$/$MoS_2$ [66], $WSe_2$/$MoSe_2$ [67], $ReS_2$/$ReSe_2$ [68], GaTe/$MoS_2$ [69], and f ranckeite/$MoS_2$ [70] were also explored to understand the photovoltaic study. Those *p-n* junctions exhibited good rectification ratio upto $10^7$ [71, 72] and large fill factor values [73]. However, introduction of graphene layer as top and bottom electrode of a *p-n* heterojunction further improves the photovoltaic response.

## 5 Lateral *p-n* junction heterostructure solar cells

Recently, lateral heterostructures are another growing interest in photovoltaic *p-n* junction fabrication, where the junction forms between *n*- and *p*-region joined laterally or induced electrostatically with a small separation distance. We will discuss in this section two different lateral *p-n* junction devices (1) CVD grown or epitaxially grown large-scale lateral *p-n* junction and (2) electrostatically induced *p-n* junction. However, fabrication of the lateral heterojunction is challenging from the synthetic point of view. To fabricate this type of lateral heterojunction devices, one has to follow the bottom-up synthesis technique [74] or electrostatically induction technique [75, 76].

Tsai et al. [77] demonstrated the fabrication of atomically sharp $WSe_2/MoS_2$ single-layer lateral heterojunction through chemical vapor deposition (CVD) method and explored the photovoltaic effect. The results are presented in Fig. 7. They obtained sharp junction between $WSe_2$ and $MoS_2$ shown in STEM image of Fig. 7a. The PL spectrum in Fig. 7c reflects the single-layer materials. They measured the current-voltage (*I-V*) characteristic of the junction using two cells (two separate junctions) and also placing them in parallel using AM 1.5G illumination. The measured current in parallel connection is just the sum of two cells' (junctions) current that can be seen from Fig. 7d. The $V_{oc}$ value remains unchanged during parallel measurements. The obtained FF from this lateral *p-n* junction devices was 40% at illuminated power ~ 200 W/m$^2$ and slowly decreases to ~ 35% at 1600W/m$^2$. The authors estimated the power conversion efficiency (PCE) from this lateral heterostructure was 2.56% under AM 1.5 illumination. Many vertical heterostructure–based photovoltaic measurements reported low efficiency due to the serious radiative recombination of spatially indirect excitons at the vertically stacked vdW interfaces [78]. Similar lateral *p-n* junction photovoltaic response and CMOS inverter was reported on $WS_2/WSe_2$, grown via CVD process by Duan et al. [79].

Sequential growth of more than one 2D materials using CVD method is one of the route to achieve large scale fabrication of the lateral *p-n* junction devices. Here, we discussed a photovoltaic performance of bilayer lateral heterojunction of $MoSe_2/WSe_2$ device reported by Sahoo et al. [80]. To study the electrical characteristics of the heterojunction, the authors designed the metallic contacts in such a way so that the measurements can be done both from the individual and across the junction as well. Figure 8a shows the optical image of the lateral junction made of three concentric triangular domains of $MoSe_2/WSe_2/MoSe_2$ junction. The area under the red dotted lines highlights the triangular junction, where *h*-BN is used as an insulator to reach the inner domains of the junction (green part). The *I-V* characteristics were measured across the contact 1-2 and 4-5, showing high-current rectification behavior (shown in the Fig. 8b–c). The zoomed figure of the current rectification

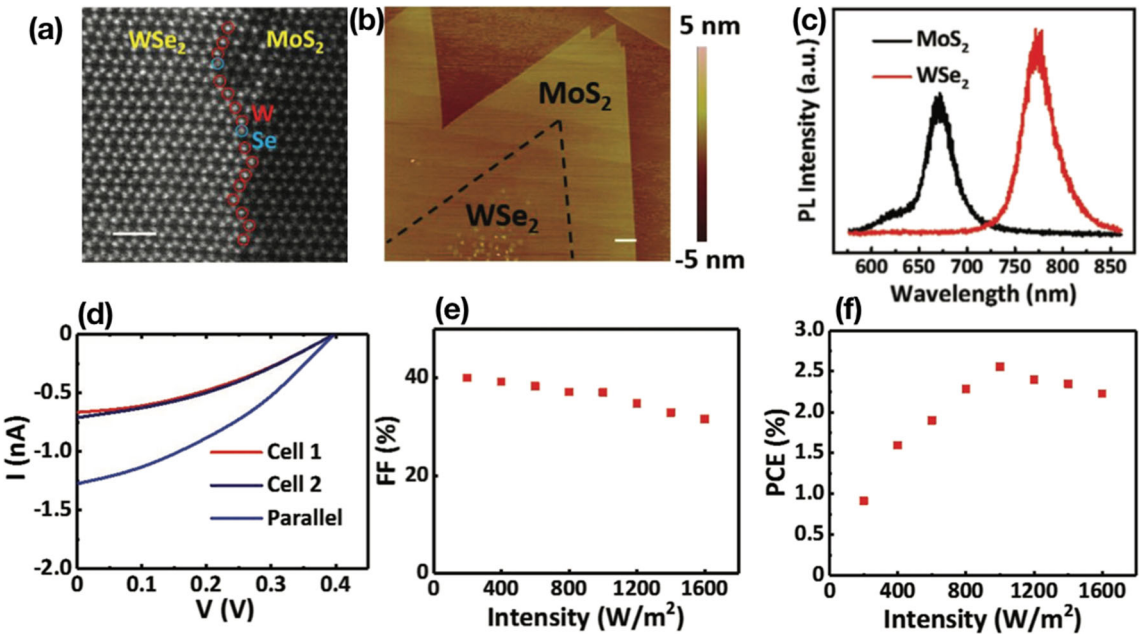


**Fig. 7** **a** High-resolution STEM image of 2D lateral $WSe_2/MoS_2$ heterojunction epitaxially grown on sapphire substrate via CVD process. **b** AFM image of monolayer $WSe_2/MoS_2$ lateral heterostructure. Scale bars are 1 nm and 1 $\mu$m in **a** and **b** respectively. **c** PL spectra of $MoS_2$ and $WSe_2$ regions. **d** *I-V* curve of the junction. Cell-1 and cell-2 are two separate junction measured and parallel is the two junction connected in parallel while doing measurements. **e** Fill-factor of the junction as a function of incident optical power using AM 1.5G illumination. **f** Power conversion efficiency as a function of incident power. Reproduced with the permission from reference [77]

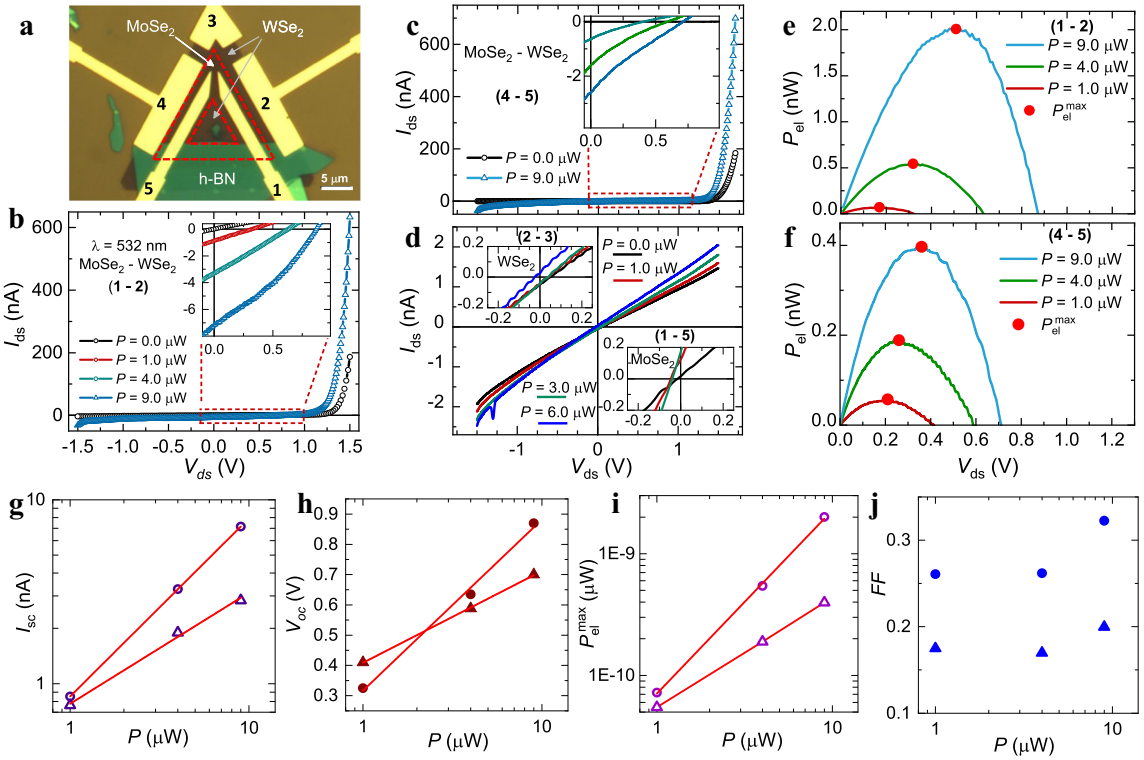


**Fig. 8** **a** Optical image of the $MoSe_2/WSe_2$ device with the gold contacts (yellow color). Red triangle part refers the device junction. **b-d** $I_{ds}$ vs $V_{ds}$ plot through the *p-n* junction and the individual domain, respectively. **e–f** Photogenerated electrical powers under different light illumination from the 1-3 and 4-5 contacts. respectively. **g–j** $I_{sc}$, $V_{oc}$, ($P_{el}^{max}$) and FF values as a function of laser illumination power, respectively. Red lines are the linear fits. Reproduced with the permission from reference [80]

in the inset of the Fig. 8b and c shows the photovoltaic responses. The $I_{ds}$ vs $V_{ds}$ measurement in the individual domain of the lateral junction (across contact 2-3 in $WSe_2$ domain and contact 1-5 in $MoSe_2$ domain) was performed (Fig. 8d) and showed absences of diode-like behavior.

Figure 8e and f display the photogenerated output electrical power at different light illuminations. The corresponding $I_{sc}$, $V_{oc}$, maximum photogenerated electrical power ($P_{el}^{max}$) and fill factor (FF) as a function of illumination power of the heterojunction are shown in Fig. 8g–j, respectively. Though $I_{sc}$ is not that high, one can see the $V_{oc}$ of the device reached to 0.9 V. Due to many extrinsic effect such as quality of contacts and the device, the extracted photovoltaic efficiency from the device was very poor $\eta = 0.08\%$.

## 6 Electrostatically induced *p-n* junction photovoltaic solar cells

Besides the vertical and lateral *p-n* junction heterostructure made of two different 2D crystals, *p-n* homojunctions based on a single 2D material were also reported by several research groups by electrostatic doping technique [76, 81, 82]. Pospischil et al. [83] illustrated the electrostatically doped $WSe_2$ homojunction where they used a split gate electrode to form the *p-n* junction. However, the PCE of ~ 0.5% was achieved for this $Wse_2$ device which is quite lower compared to the above-discussed vertical heterojunction devices. Again, *p-n* homojunction devices can also be fabricated by chemically doping the 2D crystal and this method is used to developed *p-n* junctions with 2D materials including transition metal dichalcogenides (TMDCs) [63], bP [84], and graphene [85]. The photovoltaic response of a few layered $MoSe_2$ *p-n* homojunction stacked on the dielectric *h*-BN is demonstrated by Memaran et al. [75]. The authors illustrated that the device showed a diode-like response with an photovoltaic efficiency exceeding 14% under AM 1.5 solar spectrum.

The optical image of the 10 atomic layered $MoSe_2$ flake stacked on *h*-BN is shown in Fig. 9b which was placed on a previously patterned dual gate structure on a $SiO_2/p$-Si substrate. Figure 9a shows the schematic representation of the $MoSe_2$ device configuration where one can see the dual back gates $V_{bg1}$ and $V_{bg2}$ are separated by 100–200 nm apart underneath *h*-BN forms the junction. The source and drain are connected across the junction. The absolute value of drain to source current ($I_{ds}$) as a function of applied excitation voltage $V_{ds}$ is displayed in Fig. 9c at applied back gate voltage of $V_{bg1} = -V_{bg2} = \pm 6$ V. The device

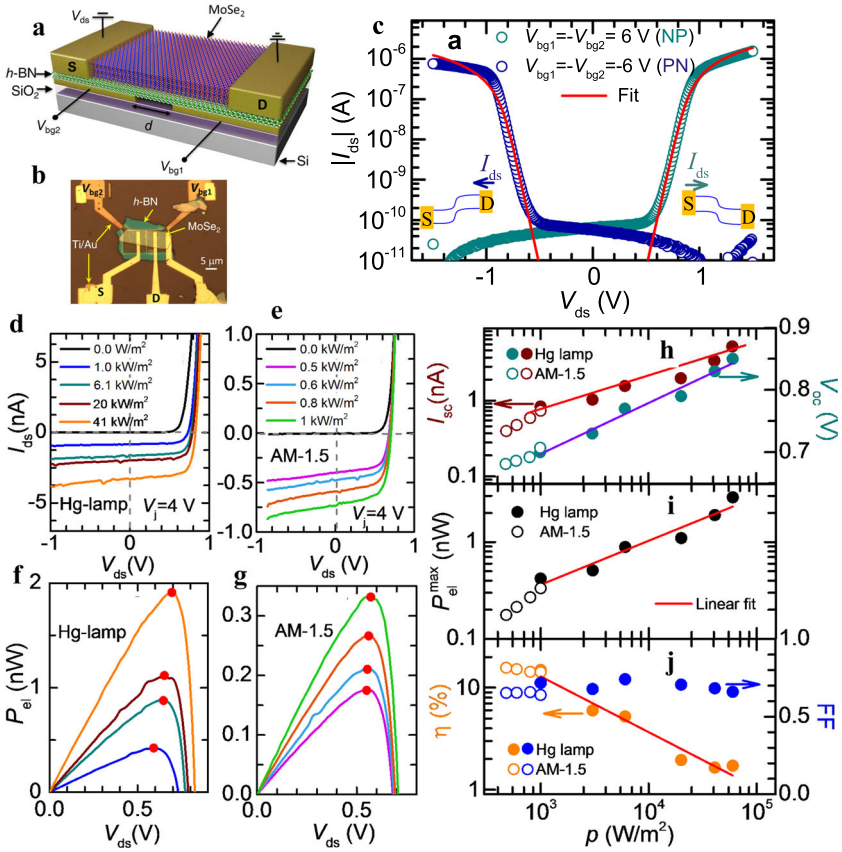


**Fig. 9** **a** Schematic representation of the device under measurement configuration. **b** Optical image of ~ 10-nm-thick $MoSe_2$ layer stacked on *h*-BN on a patterned dual gate structure. **c** $I_{ds}$ vs $V_{ds}$ plot for NP (dark cyan color) and PN configuration (blue color). Output characteristics of $MoSe_2$ device **d** under Hg lamp and **f** under AM 1.5 solar spectrum light, in the back gate voltage range +4 V to −4 V. **f**, **g** Corresponding photogenerated electrical powers from the devices under Hg lamp and AM 1.5 solar spectrum, respectively. **h** Measured short circuit current ($I_{sc}$) and open circuit voltage ($V_{oc}$). **i** Electrical power ( $P_{el}^{max}$) and **h** presents the fill factor (FF) and efficiecny ($\eta$) for the device under Hg lamp and AM 1.5 solar spectrum. Reproduced with the permission from reference [75]

showed an exact diode-like rectification of current for both NP and PN configurations. Red lines are the theoretical fit to the diode equation. Photovoltaic measurement was done using both white light Hg lamp as well as AM 1.5 light illumination and presented in Fig. 9d–j. The $I_{ds}$ vs $V_{ds}$ plots were displayed in Fig. 9d and e using Hg light and AM 1.5 respectively in NP diode configuration at constant back gate voltage $V_{bg1} = -V_{bg2} = \pm 4$ V. The $I_{sc}$ values significantly increase as a function of intensity of light illumination for both under Hg lamp as well as AM 1.5 spectrum keeping the $V_{oc}$ values nearly constant. The corresponding photogenerated electrical powers ($P_{el}$) extracted from $I_{ds}$-$V_{ds}$ measurements are presented in Fig. 9f and g for Hg lamp and AM 1.5 light respectively. The maximum output electrical power ($P_{el}^{max}$) difference in Hg lamp and AM 1.5 measurements are different due to the different power of the light intensity used. The maximum $V_{oc}$ measured in this multi-terminal $MoSe_2$ *p-n* junction device is 0.85 V at 41 kW/m$^2$ input optical power of Hg lamp. The fill factor of the device is 0.6–0.7 for both Hg lamp and AM 1.5 light illumination (Fig. 9j). The $\eta$ value for the $MoSe_2$ *p-n* homojunction device was obtained as 14% under AM 1.5 light source. The $\eta$ value for this device is much higher than the maximum values observed from the reported monolayers from the similar *p-n* junction devices [76, 82].

A similar *p-n* junction based on few layered bP with dual back gates separated by 300 nm was reported by Buscema et al. [86]. The bP *p-n* junction shows photovoltaic effect up to the near infrared (NIR) region of the solar spectrum. Authors investigated the light harvesting and photodetection behavior of the bP heterojunction device using wavelength of 640 nm as well as 808, 885, and 940 nm which shows promising photovoltaic response. The measured photovoltaic effect up to 940-nm illumination indicates that the bandgap of the bP flake is smaller than 1.31 eV and demonstrates energy harvesting in NIR part of the spectrum. This constitutes a strong advantage with respect to other 2D semiconductors such as Mo- or W-chalcogenides whose large bandgap (> 1.6 eV) limits their applicability in the NIR region [87–89].

Lastly, we are discussing a new type of lateral *p-n* junction photovoltaic device using ferroelectric materials coated the 2D semiconductor $MoTe_2$ channel [90]. The polarization of the ferroelectric film can be controlled using an AFM tip. Figure 10a presents the schematic of the device with polarization method of the ferroelectric film which causes the doping on the $MoTe_2$. Coated P(VDF-TrFE) ferroelectric film was polarized up when the conductive probe was scanned over the surface of the ferroelectric film with a negative bias voltage. The ferroelectric polarization takes advantage of the nonvolatility of electrostatic fields

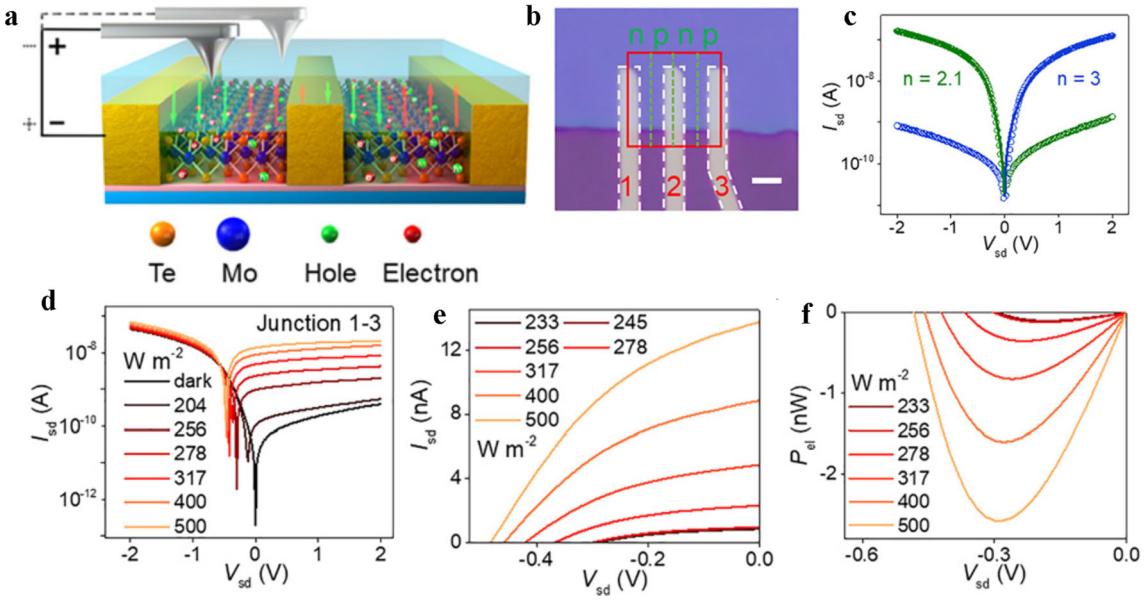


**Fig. 10** **a** Schematic of series *p-n* junction photovoltaic cells using $MoTe_2$ covered with ferroelectric materials, Poly(vinylidene fluoride) with trifluoroethylene (P(VDF-TrFE)). *p* and *n* junctions are defined by ferroelectric domains with applied electric field using AFM tip. **b** Optical image of the device with marked *n* and *p* regions. **c** *I-V* curve of the *p-n* junction device. The left and right $MoTe_2$ channels, the *n–p* junction in green line corresponds to the left channel (between contacts 1 and 2), while that in blue line refers to the right channel (between contacts 2 and 3). The electrode 2 was kept grounded. **d** *I-V* curve at several illuminated optical power density measured between the contacts 1 and 3. **e** The zoomed-in view of *I-V* curve presented in (**d**). **f** Extracted electrical output power of the device. Reproduced with the permission from reference [90]

at the interface to dope $MoTe_2$ underneath. Holes were injected into the $MoTe_2$ channel to screen the polarization field in the $P_{up}$ state, and thus, a hole-doped $MoTe_2$ was created. Similarly, if the applied bias voltage on the AFM tip will switch to positive, then the scanning area of ferroelectric domain will change to polarization-down that will induce the electron doping in the $MoTe_2$ channel. In this way, one can have *n*- and *p*-type regions on $MoTe_2$ channel to form *p-n* or *n-p* junctions. Between each pair of contacts, one can see *n*- and *p*- regions connected to each other to form the junctions. Using this method, one can make multiple *p-n* junctions connected in series shown in Fig. 10b. The FET characteristic measured after inducing *p-n* junction shows ambipolar behavior. Rectification is the important characteristic of *p-n* junction diode. Figure 10c presents the output diode characteristics for both the left and right $MoTe_2$ channels, where the *n-p* junction in the green line corresponds to the left channel, while that in blue line refers to the right channel (electrode 2 is kept grounded). The solid lines are the fit to the Shockley diode equation yields the ideality factors of the diodes are 2.1 and 3 as shown in the Fig. 10c. By shining the light, each *p-n* junction device for both sides of $MoTe_2$ will show strong photovoltaic effect. Figure 10d–f present the photovoltaic characteristic of the series connected *p-n* junction device measured between contacts 1 and 3. The *I-V* characteristic measured at dark condition and under different intensity of light from 204 to 500 W/m$^2$ shows photovoltaic response with increasing $I_{sc}$ and $V_{oc}$. The zoomed-in view of the photovoltaic response is shown in the Fig. 10e. Figure 10f presents the output electrical power from the *p-n* junction estimated from Fig. 10e, $P_{el} = I_{sd} \times V_{sd}$, at different illumination powers. The maximum electrical power ($P_{el,max}$) of $\sim$ 2.6 nW was obtained under 500 W/m$^2$ illuminated power at $V_{ds}$ = 0.3V. The power conversion efficiency ($\eta$) is calculated to be 2.8% at the illumination power of 500 W/m$^2$, which is better than the most reported 2D photovoltaic cells consisting single or bilayer 2D materials [77, 80, 83]. The fill factor (FF) is another important figure of merit calculated to be 40% from the above measurements. The photovoltaic *p-n* junction cells discussed above which was defined by ferroelectric domains could be interesting if this can be scaled to large-scale device fabrication.

We would like to emphasize here that one of the simultaneous photoeffects which generally happens in the photovoltaic devices, particularly in 2D semiconductor based devices, is the photogtaing effect. Photogating effect is generally observed in semiconductor where defects or disorder density are high [91, 92]. 2D semiconductors have high defect density. In photogating effect, *e-h* pairs generated by the incident light and one of the charge carriers, for example, in *n*-type semiconductor,

minority carrier holes can trapped at the defect sites and only photogenerated electrons will contribute the photocurrent when the drain-source voltage is applied. These trapped holes will generate an extra gate voltage in the photodiodes or phototransistors. However, in the *p-n* junction photovoltaic effect, photogenerated *e–h* pairs are separated by an internal electric field. The electric field induces the electrons and holes in a junction attached together. The origin of the internal electric field induces due to the diffusion of the electrons and holes at the junction is the *p-n* junction or a Schottky barrier at the interface between a semiconductor and a metal can serve also as *p-n* junction solar cells. The internal electric field separates the photoexcited *e–h* pairs thereby generating a sizable short-circuit current at $V_{ds}$ = 0V. The photovoltaic effect depends upon the carrier recombination process. The lower the carrier recombination, the higher the photovoltaic efficiency. Even though photovoltaic effect is a different process than photogating effect, however in defect-mediated sample, the carrier recombination process increases due to the trap of the minority carriers, which acts like an internal electric field. Thus, the photogating effect definitely has some influence on the photovoltaic effect particularly in defect-mediated photovoltaic solar cells.

In addition to the photovoltaic effects that we discussed in several examples in different configurations, each photovoltaic *p-n* junction device shows other interesting optoelectronic properties such as high rectification of diodes [75, 76], optoelectronic switches [93], and LEDs [61, 76, 94]. The diode rectification characteristic has many other applications in addition to create a photovoltaic effect. The forward bias diode has been applied in LED, logic gates used in computers, rectifiers, inverters, and TV receivers as well as used in detector and demodulator circuits. The *p-i-n* photodiodes have wide application in communication system. A unique type of optoelectronic switch was observed in few layered $MoSe_2$ transistors when illuminated with optical signal [93]. The simple ambipolar $MoSe_2$ device (without conventional *p-n* junction) shows perfect diode-like rectification in forward bias at positive applied gate voltage $V_{bg}$ = +7.5 V and with optical illumination. This forward rectification of the diode-like rectification of the device completely alters to reverse bias direction when the gate voltage switched to $V_{bg} = -7.5$ V. This behavior of altering rectification direction of a phototransistor governed by the modulation of Schottky barrier height of the device under the influence of illuminated optical signal can be used for optical switching devices where any signal need to be changed from one direction to the other by applying a gate voltage to the device. There are several reports over the past few years based on the logic gates application by these 2D semiconductor devices. The rectification of the device can be used in different combination of *n-p* or *p-n* diodes to use in logic gates design.

## 7 Challenges and opportunities

In this review, we presented the holistic view of the research in photovoltaic solar cells based on 2D materials, which provides a broad platform to understand basic fundamental properties and practical applications. Two -dimensional materials show promising application for the next-generation photovoltaic devices due to their unique optoelectronic properties. The strong light-matter interaction, and flexible and transparent nature suitable for wearable energy generation devices could be useful for many application where bulk materials may not be appropriate. However, the efficiency so far reported in these materials are very low for suitable practical applications and these studies as we can see in the Table 1 are the progress toward achieving the goal for the potential application. So far, the reported efficiency of the photovoltaic devices based on 2D materials are 1–3% or less in single-layer devices, which is far less than the efficiency of perovskite solar cells ($\eta$=15–25%) [95–98] and commercially available Si-solar module [99, 100]. Solar cells based on two dimensional materials are quite different compared to the perovskite and Si-solar cells, thus can be used in many different ways from wearable devices to thin-transparent and flexible devices. The heterostructure of 2D devices which consists of more than one layer could enhance the efficiency of solar cell compared to the devices consist of single 2D layer due to the increased absorption. However, there are many challenges which limit the realization of practical photovoltaic solar cells such as integration of the layers, measurement schemes, collection of the carriers from the cells, and selecting the appropriate combination of the 2D materials in heterostructure and contact resistance. Therefore, many systematic studies need to be done to address the above issues in the coming years which will provide tremendous opportunities for practical application of 2D material–based optoelectronic devices.

So far, many studies on 2D photovoltaic effect have been carried out using exfoliated crystals grown via CVT method due to their better quality over CVD-grown crystals. Thus, there are still challenges to grow the high-quality, large-scale 2D crystals via CVD technique which can realize large-scale practical applications. The 2D crystals with opposite polarity need to be grown top of one another to realize heterostructure fabrications. Though there are few reports of vertical and lateral heterostructure fabrication of 2D materials using CVD process, the quality and synthesis in large-scale production are still lacking. The density of

**Table 1** Photovoltaic metrices of p-n junctions based on 2D heterostructures

| PV materials ($L$ or $nm$) | Heterostructure type | λ ($nm$) | Rectification ratio | $V_{OC}$ ($V$) | $I_{SC}$ ($nA$) | $FF$ | $EQE$ (%) | $PCE$ (%) | Ref. |
|---|---|---|---|---|---|---|---|---|---|
| $MoS_2/WSe_2$ 1L/1L | Vertical | White | 50 | 0.55 | 0.025 | 0.5 | 1.5 | 0.2 | [58] |
| $MoS_2/WSe_2$ 13L/2L | Vertical | 514 | 15 | 0.27 | 220 | – | 12 | – | [59] |
| $MoS_2/WSe_2$ 1L/1L | Vertical | 532 | – | 0.5 | 70 | – | 2.4 | – | [61] |
| $bP/WS_2$ ML/ML | Vertical | AM 1.5 | $10^3$ | 0.23 | 80 | – | – | 4.6 | [62] |
| $MoTe_2/MoS_2$ 4L/4L | Vertical | 800 | $4 \times 10^3$ | 0.3 | 200 | – | 6 | – | [66] |
| $WSe_2/MoSe_2$ 3L/3L | Vertical | 633 | $10^4$ | 0.46 | > 0.04 | – | 0.02 | – | [67] |
| $ReS_2/ReSe_2$ 64/48 | Vertical | White | $3.15 \times 10^3$ | 0.175 | 0.028 | 0.37 | 4.76 | 0.48 | [68] |
| $GaTe/MoS_2$ 14.1/5.5 | Vertical | 473 | $4 \times 10^5$ | 0.22 | 1.8 | 0.42 | 61.68 | 0.45 | [69] |
| $Franckeite/MoS_2$ 25/1.4 | Vertical | 885 | 400 | 0.077 | 0.05 | – | – | – | [70] |
| $WSe_2/SnS_2$ 1L/1L | Vertical | 520 | $10^7$ | – | – | – | – | – | [71] |
| $WSe_2/MoS_2$ 25/18 | Vertical | 532 | $10^6$ | 0.4 | 40 | – | – | – | [72] |
| $BP/MoS_2$ 11/0.9 | Vertical | 633 | $10^5$ | 0.3 | 20 | 0.5 | 0.3 | 0.57 | [73] |
| $AuCl_3$ doped $MoS_2$ 3 | Vertical | 655 | 100 | 0.6 | 5.1 | 0.22 | – | 0.4 | [63] |
| $WSe_2/MoS_2$ 1L | Lateral | White | – | 0.22 | 0.008 | 0.39 | – | 0.2 | [74] |
| $WSe_2/MoS_2$ 1L | Lateral | AM 1.5 | – | 0.39 | 0.71 | 0.37 | – | 2.56 | [77] |
| $WS_2/WSe_2$ ML | Lateral | 514 | – | 0.47 | 1.2 | – | 9.9 | – | [79] |
| $MoSe_2/WSe_2$ 21 | Lateral | 532 | $10^2$ | 0.9 | 9.8 | 0.2 | – | 0.08 | [80] |
| $MoSe_2$ 10 | Lateral | AM 1.5 | – | 0.364 | 0.61 | 0.7 | – | 14 | [75] |
| $WSe_2$ 1L | Lateral (electrostatic) | White | $5 \times 10^2$ | 0.85 | 0.014 | 0.5 | – | 0.5 | [83] |
| $WSe_2$ 1L | Lateral (electrostatic) | 522 | $1 \times 10^5$ | 0.72 | 1.8 | – | 0.2 | – | [76] |
| bP 6.5 | Lateral (electrostatic) | 640 | 11 | 0.05 | 0.86 | 0.1 | 0.05 | – | [86] |

defects at the interface could be one of the challenging issues in CVD-grown crystal to form sharp high-quality *p-n* junctions, which is the main criteria for high-efficiency solar cells.

Increasing absorption in single to few atomic-layered materials is one of the important factors for improving the efficiency of the 2D material–based solar cells [101–104]. Metal nanoparticles/nanostructures exhibit strong

light-matter interaction properties with 2D nanosheets by utilizing the near-field enhancement from plasmonic excitation [53, 105–107]. Absorption cross-section can be tuned via manipulating the size of the nanostructures, which can trap the charges for longer and inject them to the 2D surface. In all the configurations of photovoltaic solar cells discussed above, plasmonic enhancement will be a potential route to enhance photocurrent efficiency.

Another challenging aspect of 2D phtotovoltaic solar cells is the collection of charge carriers very effectively or with minimum loss. Charge carriers are generated at the junction between two layers of 2D materials with opposite charge carriers in vertical or in lateral heterostructure under optical illumination. Then, the generated electron and hole pairs were separated and collected by the electrodes. Many generated charge carriers suffer in recombination process or scattering with extrinsic effects within the materials limits the efficiency of the photovoltaic cells. For a heterojunction solar cells where the contacts are away from the junction (Fig. 1a and d), electrons and holes need to move laterally from the junction to be collected. The low charge carrier mobility in the lateral transport channel results in a diffusion time for the majority carriers to leave the junction region for a small time ($\sim 1\ \mu$s for single layer heterojunction [61]), a timescale comparable to the interlayer recombination lifetime. Because photocurrent collection competes with interlayer recombination, thus the collection of charge carriers decreases in lateral collection in case of Fig. 1a and d. To enhance the carrier collection, the metal contacts need to either be as close as possible to the junction or be placed on the top of the junction as shown in the Fig. 1b. In this case, the generated electron and hole pairs can be directly collected by the graphene layers when they leave the semiconductor layer.

Contact resistance is one of the major problem in transport properties of the 2D material–based devices [108]. The rate of charge carrier injection from semiconductor to metal depends upon the quality of the semiconductor and metal interface [65, 109–112]. One has to use 2D metallic contacts such as graphene- [113–115] and $NbSe_2$-based contacts [116–118]. The band alignment on the metal and semiconductor junction is also an important factor for charge carrier injection. A low work function metal contact having the Fermi level aligned close to the conduction band of the 2D material will facilitate electron injection, whereas a high work function metal with the Fermi level aligned close to the valence band of the 2D material will prefer hole injection. Such metal-2D contacts are characterized by Schottky barriers and has been explored intensively. Fermi level pinning (FLP) is another issue for low charge carrier injection or low performance of the photovoltaic cells. Fermi level pinning degrades the performance of transistor or photovoltaic solar cells drastically because it is a parasitic resistance that burns energy while doing nothing useful. Fermi level pinning occurs at metal-semiconductor interfaces, which creates an energy barrier for the charge carriers to conduct by bending the bands at the interface between semiconductor and metal. There could be several reasons for this Fermi level pinning between the semiconductor and metal junction. The surface states caused by the incomplete covalent bonds due to the defect and impurities at the surface and 2D semiconductor are one of the reasons for the FLP. A recent study suggests that metal-induced gap states (MIGS) are the origin for the large FLP in transition metal dichalcogenides [119]. Thus, ohmic contacts is necessary to reduce the contact resistance and Fermi level pinning for improving the photovoltaic performance. Despite the defcets in the materials, several studies are proposed to reduce FLP in transition metal dichalcogenides, such as the use of buffer layers [120] or the use of other van der Waals 2D materials as the contact material [121].

Electrostatic lateral *p-n* junction has yield higher efficiency [75] in multilayered devices (Fig. 1c) due to the higher absorption and sharp junction area. But the device fabrication is not a viable process for large-scale production of devices due to complex geometry of device structure. In the other hand, this *p-n* junction could be useful for electroluminescence device [82]. The lateral *p-n* junction formed by CVD grown process shown in Fig. 1d is the desired method for large-scale production of *p-n* junction devices in single or bi-layer form but the quality of the CVD-grown materials and the junctions are not that much high quality, which limits the photovoltaic applications. Thus, more controllable, high-quality synthetic route could be developed. The vertical heterostructure with direct metal contacts on the top of the junction could be one of the most desired 2D material–based photovoltaic solar cells if the above-mentioned challenges can be addressed. Growing large-scale vertical heterostructure with different bandgap of materials could be a challenging task but a suitable, low-cost transfer process for large size crystals will lead to better 2D-based photovoltaic solar cells. Thus, there are tremendous opportunities to develop 2D material–based photovoltaic solar cells by improving the synthesis of high-quality large-scale layered semiconductors, designing heterostructure of 2D materials for high absorption of solar spectrum and engineering the solar cell devices for better performance.

## 8 Conclusion and future applications

Two-dimensional layered material shows promising applications in optoelectronics and solar cells due to their fascinating optical properties in single to few-atomic layer form.

In this article, we discussed the various aspects of phtotovoltaic *p-n* junction solar cells based on 2D materials which includes the recent development on this field in synthesis of *p-n* heterojunctions, device fabrications, and measurements. We discussed fabrication of solar cells *p-n* junction devices using mechanical transfer method from exfoliated crystals of CVT-grown materials as well as large-scale CVD-grown process. The vertical and lateral heterostructure devices with different charge collection geometries were discussed. Even though both vertical and lateral geometries are promising for future 2D photovoltaic applications depending upon the stacking feature, there are still tremendous growth opportunities to improve the efficiency of the solar cells. All the 2D photovoltaic solar cells discussed above have many challenges such as crystal quality, defects, impurities, interface quality between each layers of *p-n* junctions, and contacts. Selecting suitable bandgap 2D materials to assemble them in heterostructure for higher absorption and increasing the absorption further by integrating plasmonic nanostructure are few other suggestions. 2D materials and their heterostructures are extremely suitable for developing next-generation photovoltaic devices with flexibility, transparency, and light weight. These materials have wide range of applications in electronic portable devices, flexible transparent electronics and ceilings, and foldable battery once the efficiency of the device will be improved with minimizing the issues associated with the materials and devices.

**Funding** The authors would like to acknowledge the financial support from NSF PREM through NSF-DMR#1826886 and HBCU-UP Excellence in research NSF-DMR#1900692.

## Declarations

**Conflict of interest** The authors declare no competing interests.

## References

1. N.S. Lewis, D.G. Nocera, Powering the planet: Chemical challenges in solar energy utilization. Proc. Natl. Acad. Sci. **103**(43), 15729–15735 (2006)
2. N.S. Lewis, Research opportunities to advance solar energy utilization. Science 351(6271) (2016)
3. A. Polman, M. Knight, E.C. Garnett, B. Ehrler, W.C. Sinke, PPhotovoltaic materials: Present efficiencies and future challenges. Science 352(6283) (2016)
4. L. El Chaar, N. El Zein, et al., Review of photovoltaic technologies. Renew. Sustain. Energy Rev. **15**(5), 2165–2175 (2011)
5. M. Gul, Y. Kotak, T. Muneer, Review on recent trend of solar photovoltaic technology. Energy Explor. Exploit. **34**(4), 485–526 (2016)
6. A. Shah, P. Torres, R. Tscharner, N. Wyrsch, H. Keppner, Photovoltaic technology: the case for thin-film solar cells. Science **285**(5428), 692–698 (1999)
7. O. Schultz, S.W. Glunz, G.P. Willeke, Accelerated publication Multicrystalline silicon solar cells exceeding 20% efficiency. Progress in photovoltaics: Research and Applications **12**(7), 553–558 (2004)
8. T. Saga, Advances in crystalline silicon solar cell technology for industrial mass production. NPG Asia Materials **2**(3), 96–102 (2010)
9. W.S. Wong, A. Salleo, Vol. 11, *Flexible electronics: Materials and Applications* (Springer Science & Business Media, Berlin, 2009)
10. S. Hegedus, Thin film solar modules: the low cost, high throughput and versatile alternative to si wafers. Progress in Photovoltaics: Research and Applications **14**(5), 393–411 (2006)
11. K.L. Chopra, P.D. Paulson, V. Dutta, Thin-film solar cells: an overview. Progress in photovoltaics: Research and applications **12**(2-3), 69–92 (2004)
12. B. O'regan, M. Grätzel, A low-cost, high-efficiency solar cell based on dye-sensitized colloidal tio 2 films. Nature **353**(6346), 737–740 (1991)
13. M. Stefik, F.J. Heiligtag, M. Niederberger, M. Grätzel, Improved nonaqueous synthesis of tio2 for dye-sensitized solar cells. ACS nano **7**(10), 8981–8989 (2013)
14. P. Reinhard, A. Chirilă, P. Blösch, F. Pianezzi, S. Nishiwaki, S. Buechelers, A. Tiwari, Review of progress toward 20% efficiency flexible cigs solar cells and manufacturing issues of solar modules. in *2012 IEEE 38th Photovoltaic Specialists Conference (PVSC) PART 2* (IEEE, 2012), pp. 1–9
15. M.A. Green, A. Ho-Baillie, H.J. Snaith, The emergence of perovskite solar cells. Nature Photonics **8**(7), 506–514 (2014)
16. E.D. Kosten, J.H. Atwater, J. Parsons, A. Polman, H.A. Atwater, Highly efficient gaas solar cells by limiting light emission angle. Light: Science & Applications **2**(1), e45 (2013)
17. B.E. Hardin, H.J. Snaith, M.D. McGehee, The renaissance of dye-sensitized solar cells. Nat. Photonics **6**(3), 162–169 (2012)
18. P.V. Kamat, Quantum dot solar cells. the next big thing in photovoltaics. J. Phys. Chem. Lett. **4**(6), 908–918 (2013)
19. K.A. Mazzio, C.K. Luscombe, The future of organic photovoltaics. Chem. Soc. Rev. **44**(1), 78–90 (2014)
20. Q. Liu, Y. Jiang, K. Jin, J. Qin, J. Xu, W. Li, J. Xiong, J. Liu, Z. Xiao, K. Sun, 18% efficiency organic solar cells. Sci. Bull. **65**(4), 272–275 (2020)
21. K. Jin, Z. Xiao, L. Ding, D18, an eximious solar polymer!. J. Semicond. **42**(1), 010502–010502 (2021)
22. N.-G. Park, Organometal perovskite light absorbers toward a 20% efficiency low-cost solid-state mesoscopic solar cell. J. Phys. Chem. Lett. **4**(15), 2423–2429 (2013)
23. S. Mozaffari, M.R. Nateghi, M.B. Zarandi, An overview of the challenges in the commercialization of dye sensitized solar cells. Renew. Sustain. Energy Rev. **71**, 675–686 (2017)
24. H.-S. Kim, J.-Y. Seo, N.-G. Park, Material and device stability in perovskite solar cells. ChemSusChem **9**(18), 2528–2540 (2016)
25. K.S. Novoselov, A.K. Geim, S.V. Morozov, D. Jiang, Y. Zhang, S.V. Dubonos, I.V. Grigorieva, A.A. Firsov, Electric field effect in atomically thin carbon films. Science **306**(5696), 666–669 (2004)
26. K.S. Novoselov, V.I. Fal, L. Colombo, P.R. Gellert, M.G. Schwab, K. Kim, et al., A roadmap for graphene. Nature **490**(7419), 192–200 (2012)
27. M. Shanmugam, R. Jacobs-Gedrim, E.S. Song, B. Yu, Two-dimensional layered semiconductor/graphene heterostructures for solar photovoltaic applications. Nanoscale **6**(21), 12682–12689 (2014)
28. K.-E. Byun, H.-J. Chung, J. Lee, H. Yang, H.J. Song, J. Heo, D.H. Seo, S. Park, S.W. Hwang, I. Yoo, et al., Graphene for

true ohmic contact at metal–semiconductor junctions. Nano Lett. **13**(9), 4001–4005 (2013)
29. Y. Cui, L. Hong, J. Hou, Organic photovoltaic cells for indoor applications: Opportunities and challenges. ACS Appl. Mater. Interfaces **12**(35), 38815–38828 (2020)
30. Z. Liu, S.P. Lau, F. Yan, Functionalized graphene and other two-dimensional materials for photovoltaic devices: device design and processing. Chem. Soc. Rev. **44**(15), 5638–5679 (2015)
31. N.R. Glavin, C. Muratore, M. Snure, Toward 2d materials for flexible electronics: opportunities and outlook. Oxford Open Materials Science **1**(1), itaa002 (2020)
32. S. Das, D. Pandey, J. Thomas, T. Roy, The role of graphene and other 2d materials in solar photovoltaics. Adv. Mater. **31**(1), 1802722 (2019)
33. N.H. Hemasiri, S. Kazim, S. Ahmad, Reduced trap density and mitigating the interfacial losses by placing 2d dichalcogenide material at perovskite/htm interface in a dopant free perovskite solar cells. Nano Energy **77**, 105292 (2020)
34. M. Pegu, M.P.U. Haris, S. Kazim, S. Ahmad, Understanding and harnessing the potential of layered perovskite-based absorbers for solar cells. Emergent Materials, pp 1–28 (2020)
35. A.J. Mannix, B. Kiraly, M.C. Hersam, N.P. Guisinger, Synthesis and chemistry of elemental 2d materials. Nat. Rev. Chem. **1**(2), 1–14 (2017)
36. P. Miró, M. Audiffred, T. Heine, An atlas of two-dimensional materials. Chem. Soc. Rev. **43**(18), 6537–6554 (2014)
37. C.R. Serrao, A.M. Diamond, S.-L. Hsu, L. You, S. Gadgil, J. Clarkson, C. Carraro, R. Maboudian, C. Hu, S. Salahuddin, Highly crystalline mos2 thin films grown by pulsed laser deposition. Appl. Phys. Lett. **106**(5), 052101 (2015)
38. J. Tao, J. Chai, X. Lu, L.M. Wong, T.I. Wong, J. Pan, Q. Xiong, D. Chi, S. Wang, Growth of wafer-scale mos 2 monolayer by magnetron sputtering. Nanoscale **7**(6), 2497–2503 (2015)
39. Y.-T. Ho, C.-H. Ma, T.-T. Luong, L.-L. Wei, T.-C. Yen, W.-T. Hsu, W.-H. Chang, Y.-C. Chu, Y.-Y. Tu, K.P. Pande, et al., Layered mos2 grown on c-sapphire by pulsed laser deposition. Physica Status Solidi (RRL)–Rapid Research Letters **9**(3), 187–191 (2015)
40. M. Wasala, J. Zhang, S. Ghosh, B. Muchharla, R. Malecek, D. Mazumdar, H. Samassekou, M. Gaither-Ganim, A. Morrison, N.-P. Lopez, et al., Effect of underlying boron nitride thickness on photocurrent response in molybdenum disulfide-boron nitride heterostructures. J. Mater. Res, 31(7) (2016)
41. G. Siegel, Y.P.V. Subbaiah, M.C. Prestgard, A. Tiwari, Growth of centimeter-scale atomically thin mos2 films by pulsed laser deposition. APL Materials **3**(5), 056103 (2015)
42. H. Samassekou, A. Alkabsh, M. Wasala, M. Eaton, A. Walber, A. Walker, O. Pitkänen, K. Kordas, S. Talapatra, T. Jayasekera, et al., Viable route towards large-area 2d mos2 using magnetron sputtering. 2D Materials **4**(2), 021002 (2017)
43. J.M. Wofford, S. Nakhaie, T. Krause, X. Liu, M. Ramsteiner, M. Hanke, H. Riechert, J.M.J. Lopes, A hybrid mbe-based growth method for large-area synthesis of stacked hexagonal boron nitride/graphene heterostructures. Sci. Rep. **7**(1), 1–10 (2017)
44. K.S. Novoselov, A.H. Castro Neto, Two-dimensional crystals-based heterostructures: materials with tailored properties. Physica Scripta **2012**(T146), 014006 (2012)
45. V. Nicolosi, M. Chhowalla, M.G. Kanatzidis, M.S. Strano, J.N. Coleman, Liquid exfoliation of layered materials. Science 340(6139) (2013)
46. K.S. Novoselov, D. Jiang, F. Schedin, T.J. Booth, V.V. Khotkevich, S.V. Morozov, A.K. Geim, Two-dimensional atomic crystals. Proc. Natl. Acad. Sci. **102**(30), 10451–10453 (2005)
47. M. Xu, T. Liang, M. Shi, H. Chen, Graphene-like two-dimensional materials. Chem. Rev. **113**(5), 3766–3798 (2013)
48. B. Radisavljevic, A. Radenovic, J. Brivio, V. Giacometti, A. Kis, Single-layer mos 2 transistors. Nature Nanotechnol. **6**(3), 147–150 (2011)
49. D. Jariwala, V.K. Sangwan, D.J. Late, J.E. Johns, V.P. Dravid, T.J. Marks, L.J. Lauhon, M.C. Hersam, Band-like transport in high mobility unencapsulated single-layer mos2 transistors. Appl. Phys. Lett. **102**(17), 173107 (2013)
50. J.ong.-S. Rhyee, J. Kwon, P. Dak, J.H. Kim, S.M. Kim, J. Park, Y.K. Hong, W.G. Song, I. Omkaram, M.A. Alam, et al., High-mobility transistors based on large-area and highly crystalline cvd-grown mose2 films on insulating substrates. Adv. Mater. **28**(12), 2316–2321 (2016)
51. Z. Cai, B. Liu, X. Zou, H.-M. Cheng, Chemical vapor deposition growth and applications of two-dimensional materials and their heterostructures. Chem. Rev. **118**(13), 6091–6133 (2018)
52. X. Chen, X. Lu, B. Deng, O. Sinai, Y. Shao, C. Li, S. Yuan, V. Tran, K. Watanabe, T. Taniguchi, et al., Widely tunable black phosphorus mid-infrared photodetector. Nat. Commun. **8**(1), 1–7 (2017)
53. R.M. Liam Britnell, A. Ribeiro, R. Eckmann, B.D. Jalil, A. Belle, Y.-J. Mishchenko, R.V. Kim, T. Gorbachev, S.V. Georgiou, et al., Morozov Strong light-matter interactions in heterostructures of atomically thin films. Science **340**(6138), 1311–1314 (2013)
54. C. Schneider, M.M. Glazov, T. Korn, S. Höfling, B. Urbaszek, Two-dimensional semiconductors in the regime of strong light-matter coupling. Nat. Commun. **9**(1), 1–9 (2018)
55. Q.H. Wang, K. Kalantar-Zadeh, A. Kis, J.N. Coleman, M.S. Strano, Electronics and optoelectronics of two-dimensional transition metal dichalcogenides. Nat. Nanotechnol. **7**(11), 699–712 (2012)
56. A.K. Geim, I.V. Grigorieva, Van der waals heterostructures. Nature **499**(7459), 419–425 (2013)
57. R. Frisenda, A.J. Molina-Mendoza, T. Mueller, A. Castellanos-Gomez, H.S.J. van der Zant, Atomically thin p–n junctions based on two-dimensional materials. Chem. Soc. Rev. **47**(9), 3339–3358 (2018)
58. M.M. Furchi, A. Pospischil, F. Libisch, J. Burgdörfer, T. Mueller, Photovoltaic effect in an electrically tunable van der waals heterojunction. Nano Lett. **14**(8), 4785–4791 (2014)
59. R. Cheng, D. Li, H. Zhou, C. Wang, A. Yin, S. Jiang, Y. Liu, Y. Chen, Y. Huang, X. Duan, Electroluminescence and photocurrent generation from atomically sharp wse2/mos2 heterojunction p–n diodes. Nano Lett. **14**(10), 5590–5597 (2014)
60. J. Wong, D. Jariwala, G. Tagliabue, K. Tat, A.R. Davoyan, M.C. Sherrott, H.A. Atwater, High photovoltaic quantum efficiency in ultrathin van der waals heterostructures. ACS Nano **11**(7), 7230–7240 (2017)
61. C.-H. Lee, G.-H. Lee, A.M. Van Der Zande, W. Chen, Y. Li, M. Han, X. Cui, G. Arefe, C. Nuckolls, T.F. Heinz, et al., Atomically thin p–n junctions with van der waals heterointerfaces. Nature Nanotechnol. **9**(9), 676 (2014)
62. D.-H. Kwak, H.-S. Ra, M.-H. Jeong, A.-Y. Lee, J.-S. Lee, High-performance photovoltaic effect with electrically balanced charge carriers in black phosphorus and ws2 heterojunction. Adv. Mater. Interfaces **5**(18), 1800671 (2018)
63. H.-M. Li, D. Lee, D. Qu, X. Liu, J. Ryu, A. Seabaugh, W.J. Yoo, Ultimate thin vertical p–n junction composed of two-dimensional layered molybdenum disulfide. Nat. Commun. **6**(1), 1–9 (2015)
64. J. Miao, Z. Xu, Q. Li, A. Bowman, S. Zhang, W. Hu, Z. Zhou, C. Wang, Vertically stacked and self-encapsulated van der waals heterojunction diodes using two-dimensional layered semiconductors. ACS Nano **11**(10), 10472–10479 (2017)
65. N.R. Pradhan, C. Garcia, M.C. Lucking, Srimanta P., J. Martinez, Daniel R., R. Divan, A.V. Sumant, H. Terrones, J.L. Mendoza-Cortes, et al., Raman and electrical transport properties of

few-layered arsenic-doped black phosphorus. Nanoscale **11**(39), 18449–18463 (2019)
66. A. Pezeshki, S.H.H. Shokouh, T. Nazari, K. Oh, S. Im, Electric and photovoltaic behavior of a few-layer $\alpha$-mote2/mos2 dichalcogenide heterojunction. Adv. Mater. **28**(16), 3216–3222 (2016)
67. N. Flöry, A. Jain, P. Bharadwaj, M. Parzefall, T. Taniguchi, K. Watanabe, L. Novotny, A wse2/mose2 heterostructure photovoltaic device. Appl. Phys. Lett. **107**(12), 123106 (2015)
68. A.-J. Cho, S.D. Namgung, H. Kim, J.-Y. Kwon, Electric and photovoltaic characteristics of a multi-layer res2/rese2 heterostructure. APL Mater. **5**(7), 076101 (2017)
69. F. Wang, Z. Wang, K. Xu, F. Wang, Q. Wang, Y. Huang, L. Yin, J. He, Tunable gate-mos2 van der waals p-n junctions with novel optoelectronic performance. Nano Letters **15**(11), 7558–7566 (2015)
70. A.J. Molina-Mendoza, et al., E. Giovanelli, W.S. Paz, M.A. Niño, J.O. Island, C. Evangeli, L. Aballe, M. Foerster, H.S.J. Van Der Zant, G. Rubio-Bollinger, et al., Franckeite as a naturally occurring van der waals heterostructure. Nat. Commun. **8**(1), 1–9 (2017)
71. T. Yang, B. Zheng, Z. Wang, T. Xu, C. Pan, J. Zou, X. Zhang, Z. Qi, H. Liu, Y. Feng, et al., Van der waals epitaxial growth and optoelectronics of large-scale wse 2/sns 2 vertical bilayer p–n junctions. Nat. Commun. **8**(1), 1–9 (2017)
72. H.S. Lee, J. Ahn, W. Shim, S. Im, D.K. Hwang, 2d wse2/mos2 van der waals heterojunction photodiode for visible-near infrared broadband detection. Appl. Phys. Lett. **113**(16), 163102 (2018)
73. Y. Deng, Z. Luo, N.J. Conrad, H. Liu, Y. Gong, S. Najmaei, P.M. Ajayan, J. Lou, X. Xu, P.D. Ye, Black phosphorus-monolayer mos2 van der waals heterojunction p–n diode. ACS Nano **8**(8), 8292–8299 (2014)
74. M.-Y. Li, Y. Shi, C.-C. Cheng, L.-S. Lu, Y.-C. Lin, H.-L. Tang, M.-L. Tsai, C.-W. Chu, K.-H. Wei, H. Jr. He, et al., Epitaxial growth of a monolayer wse2-mos2 lateral pn junction with an atomically sharp interface. Science **349**(6247), 524–528 (2015)
75. S. Memaran, N.R. Pradhan, Z. Lu, D. Rhodes, J. Ludwig, Q. Zhou, O. Ogunsolu, P.M. Ajayan, D. Smirnov, A.I. Fernández-Domínguez, et al., Pronounced photovoltaic response from multilayered transition-metal dichalcogenides pn-junctions. Nano Lett. **15**(11), 7532–7538 (2015)
76. B.W.H. Baugher, H.O.H. Churchill, Y. Yang, P. Jarillo-Herrero, Optoelectronic devices based on electrically tunable p–n diodes in a monolayer dichalcogenide. Nat. Nanotechnol. **9**(4), 262–267 (2014)
77. M.-L. Tsai, M.-Y. Li, J.R.D. Retamal, K.-T. Lam, Y.-C. Lin, K. Suenaga, L.-J. Chen, G. Liang, L.-J. Li, H. Jr. He, Single atomically sharp lateral monolayer p-n heterojunction solar cells with extraordinarily high power conversion efficiency. Adv. Mater. **29**(32), 1701168 (2017)
78. H. Fang, C. Battaglia, C. Carraro, S. Nemsak, B. Ozdol, J.S. Kang, H.A. Bechtel, S.B. Desai, F. Kronast, A.A. Unal, et al., Strong interlayer coupling in van der waals heterostructures built from single-layer chalcogenides. Proc. Natl. Acad. Sci. **111**(17), 6198–6202 (2014)
79. X. Duan, C. Wang, J.C. Shaw, R. Cheng, Y. Chen, H. Li, X. Wu, Y. Tang, Q. Zhang, A. Pan, et al., Lateral epitaxial growth of two-dimensional layered semiconductor heterojunctions. Nat. Nanotechnol. **9**(12), 1024–1030 (2014)
80. P.K. Sahoo, S. Memaran, F.A. Nugera, Y. Xin, T.D. Márquez, Z. Lu, W. Zheng, N.D. Zhigadlo, D. Smirnov, L. Balicas, et al., Bilayer lateral heterostructures of transition-metal dichalcogenides and their optoelectronic response. ACS Nano **13**(11), 12372–12384 (2019)
81. R. Bratschitsch, Optoelectronic devices: monolayer diodes light up. Nat. Nanotechnol. **9**(4), 247–248 (2014)
82. J.S. Ross, P. Klement, A.M. Jones, N.J. Ghimire, Jiaqiang Y., D. Mandrus, T. Taniguchi, K. Watanabe, K. Kitamura, W. Yao, et al., Electrically tunable excitonic light-emitting diodes based on monolayer wse 2 p-n junctions. Nat. Nanotechnol. **9**(4), 268–272 (2014)
83. A. Pospischil, M.M. Furchi, T. Mueller, Solar-energy conversion and light emission in an atomic monolayer p–n diode. Nat. Nanotechnol **9**(4), 257–261 (2014)
84. G. Wang, L. Bao, T. Pei, R. Ma, Y.-Y. Zhang, L. Sun, G. Zhang, H. Yang, J. Li, C. Gu, et al., Introduction of interfacial charges to black phosphorus for a family of planar devices. Nano Lett. **16**(11), 6870–6878 (2016)
85. E.C. Peters, E.J.H. Lee, M. Burghard, K. Kern, Gate dependent photocurrents at a graphene pn junction. Appl. Phys. Lett. **97**(19), 193102 (2010)
86. M. Buscema, D.J. Groenendijk, G.A. Steele, H.S. Van Der Zant, A. Castellanos-Gomez, Photovoltaic effect in few-layer black phosphorus pn junctions defined by local electrostatic gating. Nat. Commun. **5**(1), 1–6 (2014)
87. O. Lopez-Sanchez, D. Lembke, M. Kayci, A. Radenovic, A. Kis, Ultrasensitive photodetectors based on monolayer mos 2. Nat. Nanotechnol **8**(7), 497–501 (2013)
88. Z. Yin, H. Li, H. Li, L. Jiang, Y. Shi, Y. Sun, G. Lu, Q. Zhang, X. Chen, H. Zhang, Single-layer mos2 phototransistors. ACS Nano **6**(1), 74–80 (2012)
89. N. Perea-López, A.L. Elías, A. Berkdemir, A. Castro-Beltran, H.R. Gutiérrez, S. Feng, R. Lv, T. Hayashi, F. López-Urías, S. Ghosh, et al., Photosensor device based on few-layered ws2 films. Adv. Funct. Mater. **23**(44), 5511–5517 (2013)
90. G. Wu, X. Wang, Y. Chen, S. Wu, H. Shen, T. Lin, J. Ge, W. Hu, S.-T. Zhang, X.J. Meng, et al., Two-dimensional series connected photovoltaic cells defined by ferroelectric domains. Appl. Phys. Lett. **116**(7), 073101 (2020)
91. Sujoy G., P.D. Patil, M. Wasala, S. Lei, A. Nolander, P. Sivakumar, R. Vajtai, P. Ajayan, S. Talapatra, Fast photoresponse and high detectivity in copper indium selenide (cuin7se11) phototransistors. 2D Materials **5**(1), 015001 (2017)
92. M. Buscema, J.O. Island, D.J. Groenendijk, S.I. Blanter, G.A. Steele, H.S.J. van der Zant, A. Castellanos-Gomez, Photocurrent generation with two-dimensional van der waals semiconductors. Chem. Soc. Rev. **44**(11), 3691–3718 (2015)
93. N.R. Pradhan, Z. Lu, D. Rhodes, D. Smirnov, E. Manousakis, L. Balicas, An optoelectronic switch based on intrinsic dual schottky diodes in ambipolar mose2 field-effect transistors. Adv. Electron. Mater. **1**(11), 1500215 (2015)
94. S.J. Haigh, A. Gholinia, R. Jalil, S. Romani, L. Britnell, D.C. Elias, K.S. Novoselov, L.A. Ponomarenko, A.K. Geim, R. Gorbachev, Cross-sectional imaging of individual layers and buried interfaces of graphene-based heterostructures and superlattices. Nat. Mater. **11**(9), 764–767 (2012)
95. M. Jeong, I.W. Choi, E.M. Go, Y. Cho, M. Kim, B. Lee, S. Jeong, Y. Jo, H.W. Choi, J. Lee, et al., Stable perovskite solar cells with efficiency exceeding 24.8% and 0.3-v voltage loss. Science **369**(6511), 1615–1620 (2020)
96. N.-G. Park, Green solvent for perovskite solar cell production. Nat. Sustainability: 1–2 (2020)
97. H. Ren, S. Yu, L. Chao, Y. Xia, Y. Sun, S. Zuo, F. Li, T. Niu, Y. Yang, H. Ju, et al., Efficient and stable ruddlesden–popper perovskite solar cell with tailored interlayer molecular interaction. Nat. Photonics **14**(3), 154–163 (2020)
98. B. Li, Q. Zhang, S. Zhang, Z. Ahmad, T. Chidanguro, A.H. Davis, Y.C. Simon, X. Gu, W. Zheng, N. Pradhan, et al., Spontaneously supersaturated nucleation strategy for high

reproducible and efficient perovskite solar cells. Chem. Eng. J. **405**, 126998 (2020)
99. S. Tepner, L. Ney, M. Linse, A. Lorenz, M. Pospischil, K. Masuri, F. Clement, Screen pattern simulation for an improved front-side ag-electrode metallization of si-solar cells. Prog. Photovolt. Res. Appl. **28**(10), 1054–1062 (2020)
100. A. Padhy, B. Vishal, P. Verma, G. Dwivedi, A.K. Behura, Fabrication of parabolic trough hybrid solar pv-t collector using a-si thin film solar cells in Indian perspective. Materials Today: Proceedings (2020)
101. F. Xiong, J. Zhang, Z. Zhu, X. Yuan, S. Qin, Ultrabroadband, more than one order absorption enhancement in graphene with plasmonic light trapping. Scientific Rep. **5**(1), 1–8 (2015)
102. T.J. Echtermeyer, L. Britnell, P.K. Jasnos, A. Lombardo, R.V. Gorbachev, A.N. Grigorenko, A.K. Geim, A.C. Ferrari, K.S. Novoselov, Strong plasmonic enhancement of photovoltage in graphene. Nat. Commun. **2**(1), 1–5 (2011)
103. H. Wang, S. Li, R. Ai, H. He, L. Shao, J. Wang, Plasmonically enabled two-dimensional material-based optoelectronic devices. Nanoscale **12**(15), 8095–8108 (2020)
104. X. Han, J. Xing, H. Xu, Y. Huang, D. Li, J. Lu, P. Li, Y. Wu, Remarkable improved photoelectric performance of sns2 field-effect transistor with au plasmonic nanostructures. Nanotechnology **31**(21), 215201 (2020)
105. Z. Liang, J. Sun, Y. Jiang, L. Jiang, X. Chen, Plasmonic enhanced optoelectronic devices. Plasmonics **9**(4), 859–866 (2014)
106. J. Lin, H. Li, H. Zhang, W. Chen, Plasmonic enhancement of photocurrent in mos2 field-effect-transistor. Appl. Phys. Lett. **102**(20), 203109 (2013)
107. P. Sriram, Y.-P. Wen, A. Manikandan, K.-C. Hsu, S.-Y. Tang, B.-W. Hsu, Y.-Z. Chen, Ha.-W. Lin, H.-T. Jeng, Y.-L. Chueh, et al., Enhancing quantum yield in strained mos2 bilayers by morphology-controlled plasmonic nanostructures toward superior photodetectors. Chem. Mater. **32**(6), 2242–2252 (2020)
108. Q. Zhang, J. Wei, J. Liu, Z. Wang, M. Lei, Q. Ruge, 2d/2d electrical contacts in the monolayer wse2 transistors: A first-principles study. ACS Applied Nano Materials **2**(5), 2796–2805 (2019)
109. P. Das, J. Nash, M. Webb, R. Burns, V.N. Mapara, G. Ghimire, D. Rosenmann, R. Divan, D. Karaiskaj, S.A. McGill, et al., High broadband photoconductivity of few-layered mos 2 field-effect transistors measured using multi-terminal methods: effects of contact resistance. Nanoscale (2020)
110. D.S. Schulman, A.J. Arnold, S. Das, Contact engineering for 2d materials and devices. Chem. Soc. Rev. **47**(9), 3037–3058 (2018)
111. C. Garcia, N. Pradhan, D. Rhodes, L. Balicas, S.A. McGill, Photogating and high gain in res2 field-effect transistors. J. Appl. Phys. **124**(20), 204306 (2018)
112. N.R. Pradhan, C. Garcia, J. Holleman, D. Rhodes, C. Parker, S. Talapatra, M. Terrones, L. Balicas, S.A. McGill, Photoconductivity of few-layered p-wse2 phototransistors via multi-terminal measurements. 2D Materials **3**(4), 041004 (2016)
113. W.S. Leong, X. Luo, Y. Li, K.H. Khoo, S.Y. Quek, J.T.L. Thong, Low resistance metal contacts to mos2 devices with nickel-etched-graphene electrodes. Acs Nano **9**(1), 869–877 (2015)
114. Y. Liu, H. Wu, H.-C. Cheng, S. Yang, E. Zhu, Q. He, M. Ding, D. Li, J. Guo, N.O. Weiss, et al., Toward barrier free contact to molybdenum disulfide using graphene electrodes. Nano Lett. **15**(5), 3030–3034 (2015)
115. T. Kim, S. Fan, S. Lee, M.-K. Joo, Y.H. Lee, High-mobility junction field-effect transistor via graphene/mos 2 heterointerface. Sci. Rep. **10**(1), 1–8 (2020)
116. X. Lv, W. Wei, P. Zhao, J. Li, B. Huang, Y. Dai, Tunable schottky contacts in mse 2/nbse 2 (m= mo and w) heterostructures and promising application potential in field-effect transistors. Phys. Chem. Chem. Phys. **20**(3), 1897–1903 (2018)
117. S.B. Son, Y. Kim, A. Kim, B. Cho, W.-K. Hong, Ultraviolet wavelength-dependent optoelectronic properties in two-dimensional nbse2–wse2 van der waals heterojunction-based field-effect transistors. ACS Appl. Mater. Interfaces **9**(47), 41537–41545 (2017)
118. H.sun.-J.en. Chuang, B. Chamlagain, M. Koehler, M.M. Perera, J. Yan, D. Mandrus, D. Tomanek, Z. Zhou, Low-resistance 2d/2d ohmic contacts: a universal approach to high-performance wse2, mos2, and mose2 transistors. Nano Lett. **16**(3), 1896–1902 (2016)
119. K. Sotthewes, R.V. Bremen, E. Dollekamp, T. Boulogne, K. Nowakowski, D. Kas, H.J.W. Zandvliet, P. Bampoulis, Universal fermi-level pinning in transition-metal dichalcogenides. J. Phys. Chem. C **123**(9), 5411–5420 (2019)
120. G.-S. Kim, S.-H. Kim, J. Park, K.H. Han, J. Kim, H.-Y. Yu, Schottky barrier height engineering for electrical contacts of multilayered mos2 transistors with reduction of metal-induced gap states. ACS Nano **12**(6), 6292–6300 (2018)
121. Y. Liu, P. Stradins, S.-H. Wei, Van der waals metal-semiconductor junction: Weak fermi level pinning enables effective tuning of Schottky barrier. Science Advances **2**(4), e1600069 (2016)